# High Sensitivity Terahertz Receivers Based on Plasmonic Photoconductors

by

Ning Wang

A dissertation submitted in partial fulfillment
of the requirements for the degree of
Doctor of Philosophy
(Electrical Engineering)
in the University of Michigan
2016

Doctoral Committee:

        Associate Professor Mona Jarrahi, Co-Chair
        Professor L. Jay Guo, Co-Chair
        Associate Professor Hui Deng
        Professor Herbert G. Winful

# ACKNOWLEDGEMENTS

I was very fortunate to come to the University of Michigan for my PhD studies. I had such a great experience here, which will be one of the most unforgettable experiences in my life.

First, I would like to express my special appreciation and thanks to my advisor Professor Mona Jarrahi. She sets an excellent example of a female scientist and professor for me. Her enthusiasm for research highly encouraged and motivated me, especially during tough times when my research progress was going slow. These research outcomes would not have been achievable without her patient guidance and constant feedback.

Second, I would like to thank my co-chair Professor L. Jay Guo, my committee members Professor Hui Deng, and Professor Herbert G. Winful for their brilliant comments and suggestions on my work. I also want to express my appreciation to all other professors, research scientists and staff I met at the University of Michigan, Ann Arbor, and the University of California, Los Angeles. Their valuable instructions, helpful discussions and full support extended my insight toward research, opened new doors to me, and let me explore different areas. I also would like to express my gratitude to my collaborators Dr. Hamid Javadi from the Jet Propulsion Laboratory for his assistance in characterizing plasmonic heterodyne receivers as well as Professor Arthur Gossard and Professor Hong Lu from the University of California Santa Barbara and Nanjing University for growing precious substrates for my devices.

# TABLE OF CONTENTS

# LIST OF FIGURES

ix

x

# GLOSSARY

| | |
|---|---|
| Hz | Hertz |
| GHz | Gigahertz ($10^9$ Hz) |
| THz | Terahertz ($10^{12}$ Hz) |
| m | Meter |
| μm | Micrometer |
| mm | Millimeter |
| nm | Nanometer |
| K | Kelvin |
| CW | Continuous wave |
| NEP | Noise equivalent power |
| SNR | Signal-to-noise ratio |
| GaAs | Gallium Arsenide |
| LT-GaAs | Low temperature grown Gallium Arsenide |
| SI-GaAs | Semi-insulating Gallium Arsenide |
| InGaAs | Indium Gallium Arsenide |
| ErAs:InGaAs | Erbium Arsenide doped Indium Gallium Arsenide |
| IF | Intermediated frequency |
| RF | Radio frequency |

# ABSTRACT

Terahertz radiation has unique properties that enable new functionalities for various imaging and sensing applications, such as security screening, bio sensing, medical imaging, and astronomical studies, etc. Despite great benefits that terahertz radiation can offer to these applications, high-power terahertz transmitters and sensitive terahertz receivers are still in demand to realize practical terahertz systems.

This PhD research focuses on high sensitivity terahertz receivers based on plasmonic photoconductors. Two types of terahertz receivers have been studied to achieve high terahertz detection sensitivity levels. The first type is photoconductive terahertz receivers, which are widely used for detecting terahertz pulses in time-domain terahertz spectroscopy systems. By utilizing plasmonic contact electrodes in photoconductive terahertz receivers, significantly higher detection sensitivities can be achieved compared to conventional photoconductive terahertz receivers that do not use plasmonic contact electrodes. The second type of terahertz receivers that have been studied is plasmonic heterodyne terahertz receivers, which can be used to detect continuous wave (CW) terahertz radiation and provide accurate intensity and frequency information simultaneously. A novel scheme for heterodyne terahertz receivers based on plasmonic photomixers is presented, which replaces the terahertz local oscillator of conventional heterodyne receivers with two wavelength tunable lasers to provide large dynamic range and broadband operation at room temperature.

# CHAPTER 1

# Introduction

## 1.1 Terahertz Radiation and its Applications

Terahertz range covers the frequencies between microwave and infrared frequencies in the electromagnetic spectrum, covering the frequency range from 0.1 THz to 10 THz (3 mm to 30 μm in terms of wavelength range). Radiation in this frequency range has many unique properties, which can be utilized for a wide variety of applications and research fields [1 - 5]. First of all, many optically opaque materials are transparent or semitransparent at terahertz frequencies. The fact that terahertz waves can penetrate into most non-conductive materials (e.g. cloth, paper, plastic, ceramics and cardboard) yet blocked by metallic objects makes terahertz radiation useful for security screening and detecting hidden weapons. Additionally, terahertz waves can excite molecular and lattice vibrations, which gives many chemicals distinct absorption fingerprints in the terahertz region. This enables chemical sensing, explosive detection, pharmaceutical and industrial inspection through terahertz spectroscopy. Moreover, unlike X-ray, terahertz radiation is non-ionizing and non-destructive. Therefore, it is safe for medical imaging applications. In fact, terahertz imaging has been already used to diagnose early-stage tooth decay with higher accuracies compared to traditional X-ray technology. Furthermore, terahertz radiation has promising potential applications in wireless communication. Although high atmospheric absorption limits the use of

terahertz radiation for long distance communication, it can still be used for short-range and high-altitude communication to achieve significantly higher data rates.

## 1.2 Motivation

Powerful terahertz transmitters and sensitive terahertz receivers are the most important components in all of the applications mentioned above. Unfortunately, conventional techniques used for generating and detecting microwave and infrared radiation do not operate efficiently at terahertz frequencies. This is because of frequency limitations of electronic devices based on transistors, which have cutoff frequencies of ~300 GHz [5], and frequency limitations of conventional semiconductor lasers restricted by the bandgap energy of natural materials. As a result, new techniques should be explored to develop high-performance terahertz transmitters and receivers in this spectral gap.

Thanks to advancements in femtosecond lasers, short-carrier lifetime semiconductor materials and nanotechnology, significant progress has been made in terahertz generation and detection techniques. The first breakthrough happened in 1980, when David Auston and his co-workers demonstrated that photoconductors are capable of generating and coherently detecting picosecond electrical pulses [6]. This was followed by demonstration of terahertz generation by using optical rectification in 1983 [7] and photoconductive antennas in 1988 [8], inspiring researchers from different areas. From that time on, many terahertz generation and detection methods have been invented, offering terahertz transmitters and receivers with improved performance [9 - 25]. In this dissertation, a new generation of photoconductive terahertz receivers based on plasmonic contact electrodes will be introduced and demonstrated, which offers significantly higher detection sensitivity levels compared to conventional photoconductive terahertz receivers. Moreover, a new

generation of heterodyne terahertz receivers based on plasmonic photomixers will be presented and demonstrated, which offers significantly broader operation bandwidths and larger dynamic ranges compared to conventional heterodyne terahertz receivers.

## 1.3 Summary of Contributions

In this PhD dissertation, two types of high sensitivity terahertz receivers are being studied and discussed. The study of plasmonic photoconductive terahertz receivers results in a novel approach for improving terahertz detection sensitivity by incorporating plasmonic contact electrodes in photoconductive antennas. The research on plasmonic heterodyne terahertz receivers leads to a powerful scheme for extending the operation bandwidth and dynamic range of heterodyne terahertz receivers. For each type of terahertz receiver, prototype devices are designed, fabricated, and characterized to experimentally demonstrate their superior performance compared to the state-of-the art. The main contributions described in this dissertation include:

- Theoretical study and analysis of responsivity and noise performance of terahertz receivers based on photoconductors;

- Specific design of plasmonic contact electrodes to enhance optical power absorption in active area of plasmonic photoconductors and photomixers and improve carrier concentration in close proximity to the device contact electrodes;

- Specific design of various terahertz antennas integrated with plasmonic contact electrodes for efficient detection of an incident terahertz radiation;

- Detailed fabrication and packaging of the prototypes plasmonic photoconductive terahertz receivers and plasmonic heterodyne terahertz receivers;

3

- Characterization of a prototype photoconductive terahertz receiver with plasmonic contact electrodes in comparison with a conventional photoconductive terahertz receiver without plasmonic contact electrodes in a time-domain terahertz spectroscopy setup and experimental demonstration of 30 fold detection sensitivity enhancement over 0.1-1.5 THz frequency band;

- Characterization of plasmonic heterodyne terahertz receiver prototypes designed for operation at different terahertz frequency bands and experimental demonstration of large dynamic range and broadband operation at room temperature;

## 1.4 Dissertation Outline

This dissertation is arranged as follows:

**Chapter 1** introduces terahertz radiation and its applications, and explains motivation for research on pulsed and CW terahertz receivers with improved detection performance. It also states the key findings of this dissertation.

**Chapter 2** discusses the state-of-the-art terahertz receivers and compares advantages and disadvantages of each type of receiver for various applications. A special emphasis is given to photoconductive terahertz receivers and heterodyne terahertz receivers, which will be further discussed in later chapters.

**Chapter 3** describes the theoretical analysis of responsivity and noise performance of terahertz receivers based on photoconductors. The results of this analysis are used for optimizing the design of high sensitivity terahertz receivers based on plasmonic photoconductors.

**Chapter 4** presents the novel idea of plasmonic photoconductive terahertz receivers for pulsed terahertz detection with enhanced detection sensitivity levels. Detailed design, fabrication and characterization of a prototype plasmonic photoconductive terahertz receiver are described and the device performance is compared with a conventional photoconductive terahertz receiver.

**Chapter 5** introduces the novel idea of plasmonic heterodyne terahertz receivers for detecting CW terahertz waves over a broad range of terahertz frequencies. Detailed design, fabrication and characterization of plasmonic heterodyne terahertz receivers are stated. Experimental results are presented and analyzed.

**Chapter 6** concludes this dissertation, provides a summary of key contributions, and gives suggestions for future research.

# CHAPTER 2

# State-of-the-Art Terahertz Receivers

Existing terahertz receivers can be divided in four major categories based on their operation mechanism: Direct receivers, heterodyne receivers, electro-optic sampling receivers and photoconductive receivers [26 - 28].

## 2.1   Direct Terahertz Receivers

This category of terahertz receivers are designed to directly sense the electric field or thermal energy associated with a received terahertz radiation. Bolometers [29], pyroelectric detectors [30], Golay cells [31, 32], Schottky diodes, and field-effect transistors are widely used as direct terahertz receivers. Direct terahertz receivers are easy to operate and can be easily incorporated in large focal plane arrays for various imaging applications [33]. Room-temperature direct terahertz receivers can provide noise equivalent power (NEP) values as low as $10^{-10}$-$10^{-9}$ W/Hz$^{1/2}$. On the other hand, cryogenic-cooled direct receivers (operating at temperatures below 4 K) can offer much higher detection sensitivity levels with NEP values of $10^{-13}$-$5\times10^{-17}$ W/Hz$^{1/2}$ [28].

## 2.2   Heterodyne Terahertz Receivers

Heterodyne terahertz receivers can provide intensity and frequency information of a received terahertz radiation and are widely used in sensing applications with high spectral resolution

requirement. A heterodyne terahertz receiver mixes a received terahertz signal with a reference local oscillator (LO) signal, down-converting it to an intermediate frequency (IF) signal, which can be accurately analyzed and detected by well-developed radio frequency (RF) instruments. This heterodyne detection process is illustrated in Figure 1. A mixer is used to mix the terahertz signal at $f_{THz}$ with a local oscillator signal at $f_{LO}$, generating an IF signal at $f_{IF} = |f_{THz} - f_{LO}|$. The IF signal is usually amplified by a low noise IF amplifier before next processing steps. Mixers and local oscillators are the key components in heterodyne terahertz receivers. Schottky diode mixers, superconductor-insulator-superconductor (SIS) mixers, and hot electron bolometer (HEB) mixers are the most commonly used mixers in existing heterodyne terahertz receivers [34 - 50].
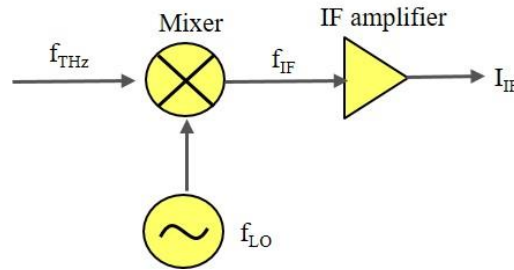


Figure 1. Schematic diagram of a heterodyne terahertz receiver.

Schottky diode mixers employ the nonlinear current-voltage (I-V) characteristic of Schottky barrier diodes to mix a terahertz signal with a local oscillator signal (Figure 2 (b)). Current at a Schottky barrier junction is the result of thermal emission, carrier tunneling and carrier generation-recombination inside and outside of the Schottky depletion region (marked as 1, 2, 3 and 4 in Figure 2 (a)). The last two mechanisms can be neglected in terahertz Schottky diodes because of low concentration of holes inside and outside of the Schottky depletion region for recombination. In order to operate efficiently as terahertz mixers, Schottky diodes are forward biased to benefit from the exponential relation between the device current and bias voltage, $V_b$. In this regime, the

combination of the incident terahertz and local oscillator signals induces a voltage variation across the Schottky barrier. This results in an exponential increase or decrease in the device current, depending on the polarity and strength of the incident terahertz field with respect to the local oscillator field. A mixing product of the incident and local oscillator terahertz signals will be induced in the Schottky diode current, accordingly. The skin effect, charge inertia, dielectric relaxation, and plasma resonances can degrade the efficiency of Schottky diode mixers. The dominant noise sources in Schottky diode mixers are the Johnson Nyquist noise associated with the Schottky diode series resistance and the shot noise associated with hot electrons [37]. Although Schottky diode mixer operation up to 25 THz has been demonstrated, low noise Schottky diode mixer operation has been achieved in frequency ranges below 5 THz [35 - 38]. Schottky diode mixers can operate at room temperature and can offer higher sensitivities if cryogenically cooled. They can offer IF bandwidths of tens of gigahertz, however, they require relatively high local oscillator power levels of several milliwatts to provide acceptable sensitivities.
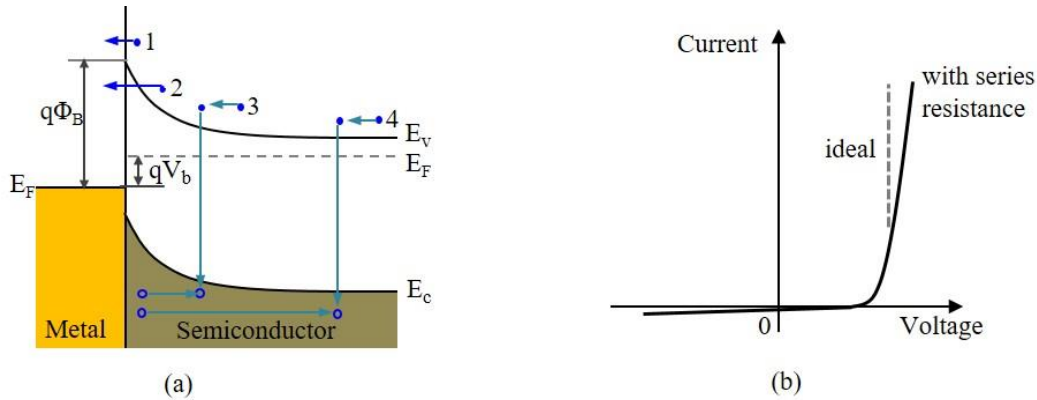


Figure 2. (a) Band diagram of a forward-biased Schottky contact with an n-type semiconductor substrate; (b) I-V characteristic (linear scale) of a Schottky barrier diode.

SIS mixers use SIS tunnel junctions as the mixing elements and can offer quantum-limited noise temperatures of $2h\nu/kT$. A SIS tunnel junction is composed of two superconductors separated by a

thin insulating layer. The SIS mixer operation is based on photo-assisted tunneling of quasi-particles through the insulating layer, as illustrated in Figure 3 (a). When a bias voltage $V_b$ is applied to the junction, an energy shift of $qV_b$ is introduced between the Fermi levels of the two superconductors. No current flows if $qV_b$ is lower than the superconductor energy gap ($2\Delta$). However, tunneling occurs if the junction is irradiated with photon energies higher than $2\Delta - qV_b$, introducing a steep current rise as the number of photons increases (Figure 3 (b)). SIS mixers require cryogenic cooling below 5 K and modest local oscillator power levels of $40 - 100~\mu W$ to provide quantum-level sensitivities. However, their operation frequency has been limited to 1.6 THz due to a reverse tunneling process at higher frequencies [39 - 44].
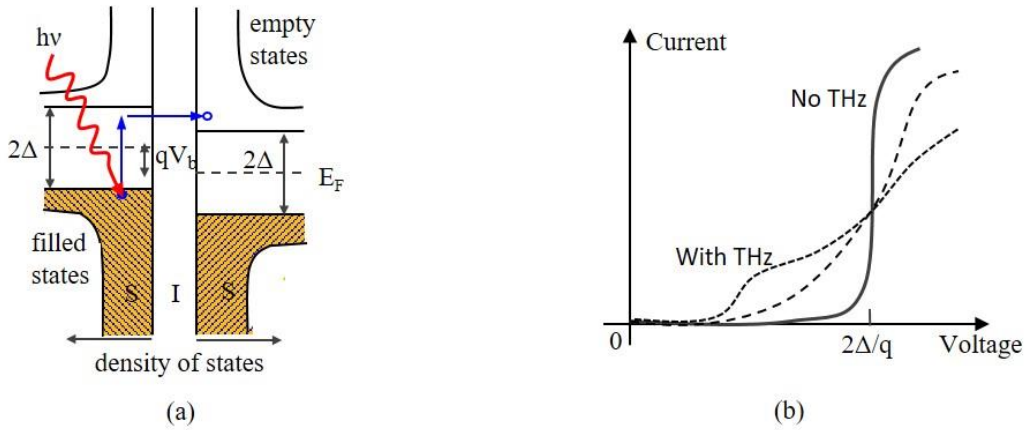


Figure 3. (a) Band diagram of an SIS junction at an applied bias voltage and illustration of photon assisted tunneling; (b) I-V characteristic of a non-irradiated and irradiated barrier.

HEB mixers use the nonlinear resistance-temperature characteristic of micro-bridge superconductors to mix a terahertz signal with a local oscillator signal. They consist of a superconductor micro-bridge integrated with a terahertz antenna, as shown in Figure 4 (a), and operate at the superconductor resistive state close to the transition temperature $T_c$. When the terahertz and local oscillator signals are coupled into the micro-bridge through the terahertz

antenna, the induced temperature changes switch the material state from superconducting to normal. This results in an abrupt change in the micro-bridge resistance. This transition is fast enough to track IF signals up to several GHz. This is because of fast electron diffusion cooling when using micro-bridge lengths shorter than the thermal diffusion length and fast phonon cooling when using micro-bridge lengths longer than the thermal diffusion length. A major advantage of HEB mixers is offering high detection sensitivities while requiring low local oscillator powers of $1 - 2$ µW. However, their major disadvantage is that they require cryogenic cooling for operation.
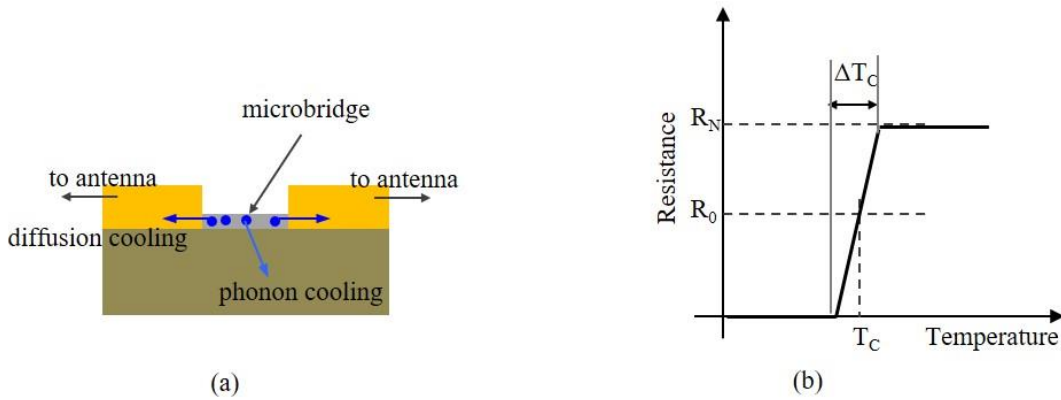


Figure 4. (a) Simplified diagram of an HEB mixer; (b) Schematic diagram of a typical superconductor resistive transition. In the mixer mode, the micro-bridge is biased at R0 and Tc.

Apart from mixers, local oscillators are another important components in heterodyne terahertz receivers. Optically pumped gas lasers are widely used as local oscillators in heterodyne receivers above 2 THz. Different terahertz gas lasers can offer radiation lines covering 150 GHz to 8 THz frequency range with output powers ranging from several microwatts up to several hundreds of milliwatts [38]. However, their limited frequency tunability prevents their usage in many applications. Multiplier-based sources are usually used as local oscillators below 2 THz and offer

sufficient output powers for pumping HEB and SIS mixers. However, the frequency tuning range of this category of sources is also limited for many spectroscopy applications.
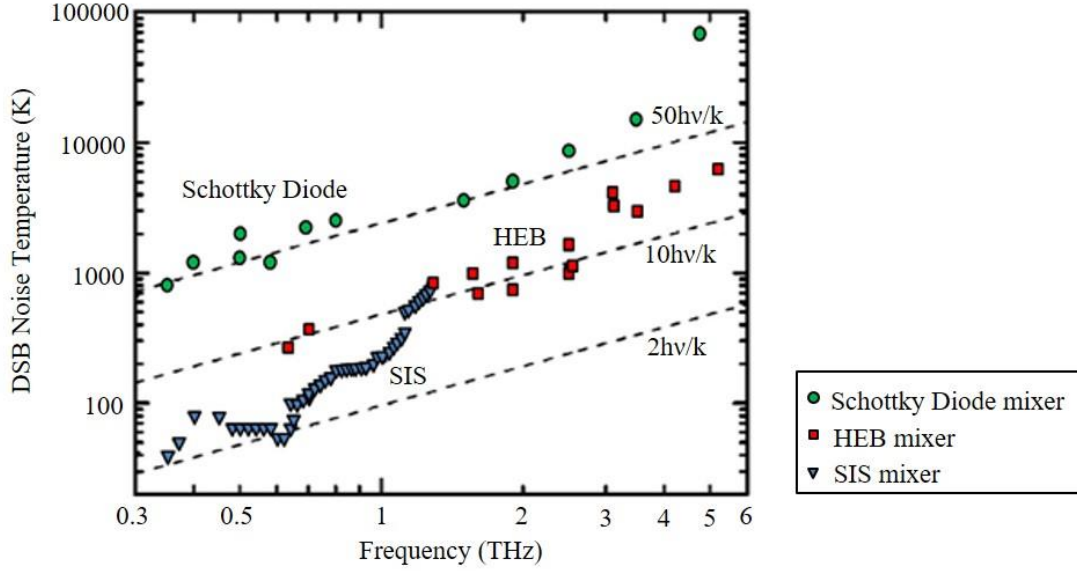


Figure 5. DSB noise temperature of demonstrated heterodyne terahertz receivers based on Schottky diode mixers, SIS mixers, and HEB mixers.

Figure 5 shows a comparison between the double sideband (DSB) noise temperature of demonstrated heterodyne terahertz receivers based on Schottky diode, SIS, and HEB mixers [50]. One of the major limitations of all of these receivers is their narrow operation bandwidth, limited by the frequency tuning range of terahertz local oscillators and mixer parasitics.

## 2.3   Electro-Optic Sampling Terahertz Receivers

Electro-optic (EO) sampling is commonly used in time-domain terahertz spectroscopy systems for detecting pulsed terahertz radiation. Crystals with strong Pockels effect (e.g. $LiTaO_3$, $LiNbO_3$, and ZnTe), which become birefringent under an applied electric field, are used for this purpose. An

incident terahertz electric field is measured by monitoring polarization changes in a probe optical beam in response to the incident terahertz electric field.
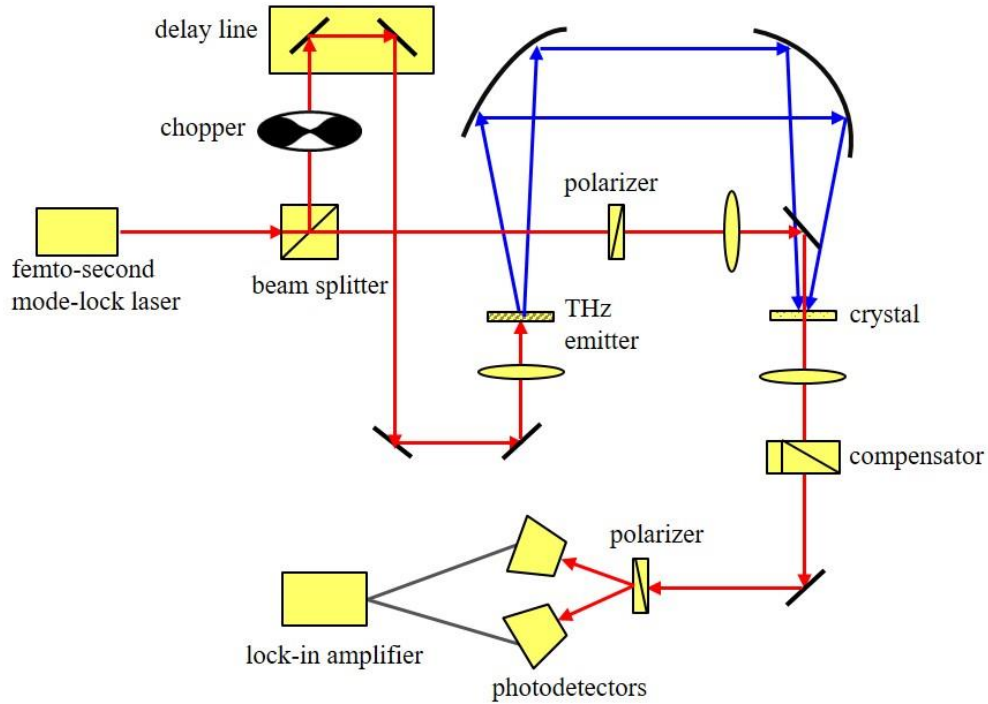


Figure 6. Schematic diagram of an exemplary electro-optic sampling terahertz receiver.

Figure 6 shows an exemplary setup for an EO sampling terahertz receiver. Femtosecond pulses from a mode-locked laser are used to pump a pulsed terahertz emitter. The generated terahertz pulses are focused onto an EO crystal for detection. A fraction of the laser beam, used as the probe beam, is also focused onto the EO crystal while overlapping with the focused terahertz beam. The incident terahertz field modifies the polarization state of the probe beam. Variations in the polarization state of the probe beam are monitored by using a Wollaston prism followed by two balanced photodetectors connected to a lock-in amplifier. The output signal is a measure of rotation in the polarization of the probe beam and the incident terahertz field, accordingly. By tuning the time-delay between the generated terahertz pulses and probe beam, the temporal waveform of the

12

terahertz electric field is measured. The temporal resolution and bandwidth of the EO sampling receiver depends on the laser pulse duration, material properties and crystal thickness. Compared to photoconductive terahertz receivers, EO sampling can offer a more broadband operation.

## 2.4   Photoconductive Terahertz Receivers

Similar to EO sampling receivers, photoconductive terahertz receivers are usually used in time-domain terahertz spectroscopy systems for detecting terahertz pulses. They consist of an ultrafast photoconductor pumped by femtosecond laser pulses. To achieve high detection sensitivities, the photoconductors should have short carrier lifetime and high resistivity properties. Photo-generated carriers inside the photoconductor substrate are drifted by an incident terahertz electric field to be detected, inducing a photocurrent. The induced photocurrent $I(t)$ is proportional to the time integral of the product of the terahertz electric field $E(t)$ and the total number of the photo-generated carriers $N(t)$: $I(t) \propto \int_{-\infty}^{+\infty} E(t')N(t'-t)dt'$. Therefore, the induced photocurrent is proportional to the incident terahertz electric field for photoconductive receivers with ultra-short carrier lifetime substrates. By tuning the time-delay between the incident terahertz beam and pump beam, the temporal waveform of the terahertz electric field is measured. Compared to EO sampling receivers, photoconductive receivers can offer superior detection sensitivity at lower terahertz frequencies. At higher frequencies, the detection sensitivity of photoconductive receivers degrades due to bandwidth limitations of terahertz antennas, limited carrier drift velocities, and photoconductor parasitics. Characteristics of photoconductive terahertz receivers will be further discussed in the following chapters.

## 2.5   Conclusion

Significant progress has been made toward enhancing detection sensitivity of various terahertz receivers. However, existing terahertz receivers have not yet provided high detection sensitivity levels, large dynamic ranges, and broad operation bandwidths required for many applications within a low-cost and compact system platform. Therefore, new terahertz detection schemes are needed to address the limitations of existing terahertz receivers. In this PhD dissertation, novel designs of photoconductive terahertz receivers with plasmonic contact electrodes and new schemes for heterodyne terahertz receivers based on plasmonic photomixers are presented and their superior performance in enhancing terahertz detection sensitivity and bandwidth is demonstrated.

# CHAPTER 3

# Analysis of Responsivity and Noise of Terahertz Receivers based on Photoconductors

Before discussing high sensitivity terahertz receivers based on photoconductors, a thorough analysis of responsivity and noise performance of photoconductive terahertz receivers is presented in this chapter. The tradeoff between low-noise and high-responsivity operation of photoconductive terahertz receivers is investigated as a function of device parameters and operational settings.

## 3.1 Evaluation Parameters of Terahertz Receivers based on Photoconductors

Performance of terahertz receivers based on photoconductors can be evaluated by parameters such as responsivity, signal-to-noise ratio (SNR), noise equivalent power (NEP) and noise temperature. Responsivity ($R$) of a photoconductive terahertz receiver is defined as the ratio of the detected photocurrent ($I_{ph}$) to the incident terahertz power ($P_{THz}$):

$$R = \frac{I_{ph}}{P_{THz}} \tag{1}$$

Noise of a photoconductive terahertz receiver includes Johnson-Nyquist noise, shot noise, and flicker noise, and is usually quantified by the root-mean-square (RMS) of the noise current.

15

Johnson-Nyquist noise, which is also called thermal noise, is the result of random motion of carriers with average energy of $k_BT$, contributing to the dark current of the device. The noise current is given by

$$i_{n-Nyquist} = \sqrt{\frac{4k_BT\Delta f}{R_s}}$$ (2)

where $k_B$ is the Boltzmann's constant, $T$ is the receiver's operation temperature in kelvins, $\Delta f$ is the receiver's bandwidth and $R_s$ is the resistance of the photoconductor. Johnson-Nyquist noise is unavoidable.

Shot noise results from random fluctuations of electric current when charge carriers transverse a gap. Shot noise in photoconductive receivers is related to the induced photocurrent and can be calculated by

$$i_{n-Shot} = \sqrt{2qI_{ph}\Delta f}$$ (3)

where q is the element charge of an electron.

Flicker noise arises from surface/interface defects and/or traps in photoconductive substrate and has a spectral noise current inversely proportional to the square root of the photocurrent frequency. Therefore, low Flicker noise levels can be maintained by modulating the output photocurrent of photoconductive terahertz receivers at high frequencies.

Therefore, signal-to-noise ratio (SNR) of a photoconductive terahertz receiver can be calculated as the ratio of the induced photocurrent to the noise current

$$SNR = \frac{i_{ph}}{\sqrt{i_{n-Nyquist}^2 + i_{n-Shot}^2}}$$ (4)

Noise-equivalent-power (NEP) and noise temperature are two measures of the receivers' sensitivity. Both of them express the minimum detectable power by the receivers. NEP is defined as the minimum power that a receiver can detect in a one hertz output bandwidth. Noise temperature is used to express the minimum detectable power spectral density in terms of temperature (in kelvins). NEP and noise temperature of a photoconductive terahertz receiver are expressed as

$$NEP = \frac{P_{min}}{\sqrt{\Delta f}} \tag{5}$$

$$T = \frac{P_{min}}{k_B \Delta f} \tag{6}$$

where $P_{min}$ is the minimum detectable power by the receiver.

## 3.2 Responsivity and Noise Analysis of Terahertz Receivers based on Photoconductors

In a photoconductive terahertz receiver, the photocurrent $I_{ph}$ is induced as a result of diffused and drifted photo-generated carriers. In the presence of a terahertz electric field, the diffusion photocurrent is much weaker than the drift photocurrent and can be neglected. To have a more accurate analysis of the responsivity and noise performance of photoconductive terahertz receivers, two general photoconductive receiver architectures, symmetrically pumped (Figure 7 (a)) and asymmetrically pumped (Figure 7 (b)) architectures, are analyzed separately. Both architectures consist of a photoconductor integrated with a terahertz antenna. The photoconductor is pumped by a pulsed or heterodyned optical pump to detect a pulsed or CW terahertz radiation, respectively. While the optical pump illuminates the entire photo-absorbing semiconductor region between photoconductor contact electrodes in the symmetric receiver architecture, the optical pump is

17

tightly focused onto a photo-absorbing semiconductor region near one of the photoconductor contact electrodes in the asymmetric receiver architecture. With the illumination of the optical pump, electron-hole pairs are generated inside the photo-absorbing substrate. Meanwhile, when an incident terahertz radiation is received by the terahertz antenna, it induces a terahertz electric field in the photoconductor active region and drifts the photo-generated carriers to the photoconductor contact electrodes. This generates an output photocurrent, which is proportional to the intensity of the received terahertz electric field.
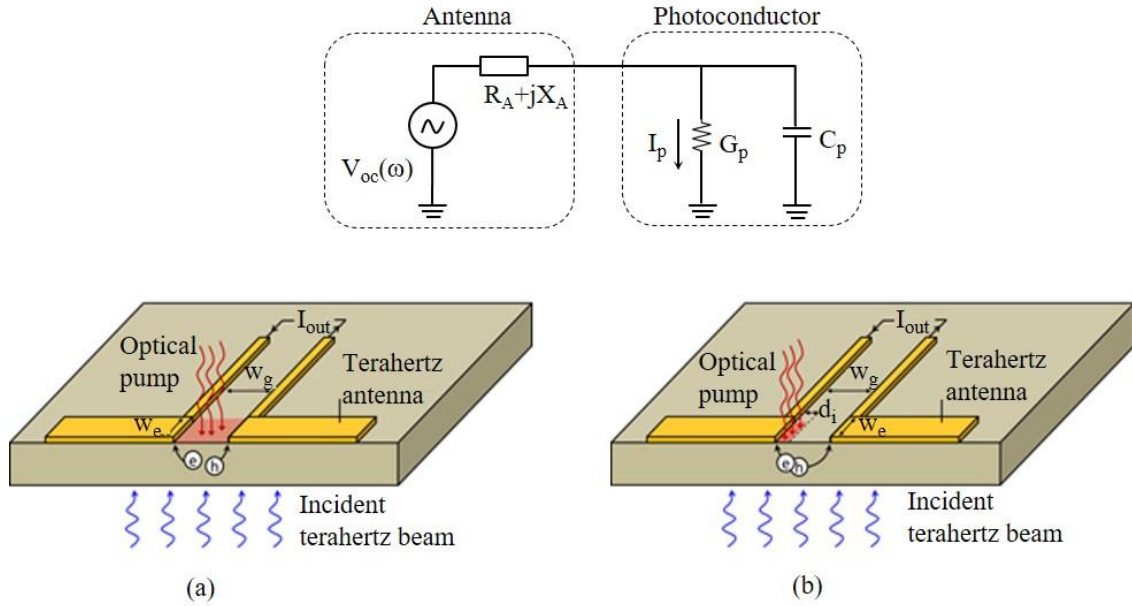


Figure 7. Schematic diagram of (a) a photoconductive receiver symmetrically pumped by the optical pump, (b) a photoconductive receiver asymmetrically pumped by the optical pump. Inset shows the equivalent circuit model of both symmetrically pumped and asymmetrically pumped photoconductive receivers.

Here the continuous-wave terahertz detection is used to derive all the parameters. This analysis can be easily extended to a continuous span of frequencies to evaluate the performance of photoconductive terahertz receivers in pulsed terahertz detection.

Assume a heterodyne optical pump is employed with its frequency difference set at the frequency of the continuous-wave terahertz radiation to be detected, offering an optical pump power envelope of

$$P_{opt} = P_0 + P_\omega sin(\omega t) \tag{7}$$

where $\omega$ is the angular frequency difference of the heterodyned optical pump, $P_0$ is the DC component of the envelope of the optical pump, and $P_\omega$ is the frequency component of the envelope of the optical pump at the angular frequency $\omega$.

### 3.2.1 Symmetrically pumped terahertz receivers based on photoconductors

In the case of the symmetrically pumped photoconductive receivers (Figure 7 (a)), if the pump photons have a uniform intensity across the photoconductor active area and are uniformly absorbed within the absorption depth, the density of electrons, $n$, and holes, $p$, generated within the photoconductor active region can be calculated from [56, 68, 69]

$$\frac{dn}{dt} = \frac{\eta_e \alpha}{hv.w_g w_e}(P_0 + P_\omega sin(\omega t)) - \frac{n}{\tau_n} \tag{8}$$

$$\frac{dp}{dt} = \frac{\eta_e \alpha}{hv.w_g w_e}(P_0 + P_\omega sin(\omega t)) - \frac{p}{\tau_p} \tag{9}$$

where $hv$ is the element energy of the pump photons, $\eta_e$ is the photoconductor external quantum efficiency (number of generated electron-hole pairs per each incident photon), $\alpha$ is the absorption coefficient of the pump photons in the photo-absorbing semiconductor, $\tau_n$ and $\tau_p$ are lifetimes of electrons and holes in the semiconductor, $w_g$ is the gap between photoconductor contact electrodes, and $w_e$ is the width of the photoconductor active region. Therefore, photo-generated carrier density inside the photoconductor active region can be calculated as [70]

$$n(t) = \frac{\eta_e \alpha \tau_n}{h\nu.w_g w_e} P_0 \left[ 1 + \frac{P_\omega sin(\omega t + \varphi_n(\omega))}{P_0 \sqrt{1 + \omega^2 \tau_n^2}} \right] \tag{10}$$

$$p(t) = \frac{\eta_e \alpha \tau_p}{h\nu.w_g w_e} P_0 \left[ 1 + \frac{P_\omega sin(\omega t + \varphi_p(\omega))}{P_0 \sqrt{1 + \omega^2 \tau_p^2}} \right] \tag{11}$$

where $\varphi_n(\omega) = \tan^{-1}(1/\omega\tau_n)$ and $\varphi_p(\omega) = \tan^{-1}(1/\omega\tau_p)$. Assuming the photo-generated carrier density inside the photoconductor active region is higher than the intrinsic carrier density of the photo-absorbing semiconductor, the photoconductor conductance can be derived from the calculated photo-generated carrier density [70, 71]

$$G_p(t) = \frac{\eta_e q \tau_n \mu_n}{h\nu.w_g^2} P_0 \left[ 1 + \frac{P_\omega sin(\omega t + \varphi_n(\omega))}{P_0 \sqrt{1 + \omega^2 \tau_n^2}} \right] + \frac{\eta_e q \tau_p \mu_p}{h\nu.w_g^2} P_0 \left[ 1 + \frac{P_\omega sin(\omega t + \varphi_p(\omega))}{P_0 \sqrt{1 + \omega^2 \tau_p^2}} \right] \tag{12}$$

where $q$ is the electron charge, $\mu_n$ and $\mu_p$ are electron and hole mobilities, respectively.

The equivalent circuit model of the photoconductive receiver is shown in Figure 7 inset, where $R_A$ and $X_A$ are the antenna radiation resistance and reactive components (including inductance of bias line), respectively, $C_p$ is the photoconductor capacitance, and $V_{oc}(\omega)$ is the open circuit voltage induced at the antenna terminal in response to the incident terahertz radiation. Using the equivalent circuit model of the photoconductive receiver, the induced photocurrent in the photoconductor can be calculated as

$$I_{p-sym}(t) = \left[ \frac{\eta_e q \tau_n \mu_n}{h\nu.w_g^2} P_0 \left[ 1 + \frac{P_\omega sin(\omega t + \varphi_n(\omega))}{P_0 \sqrt{1 + \omega^2 \tau_n^2}} \right] + \frac{\eta_e q \tau_p \mu_p}{h\nu.w_g^2} P_0 \left[ 1 + \frac{P_\omega sin(\omega t + \varphi_p(\omega))}{P_0 \sqrt{1 + \omega^2 \tau_p^2}} \right] \right]$$

$$\times \frac{V_{oc} \sin(\omega t + \varphi_0)}{1 + (R_A + jX_A)(\overline{G_p(t)} + j\omega C_p)} \tag{13}$$

where $\overline{G_p(t)}$ is the average value of the photoconductor conductance. Ultimately, responsivity of the photoconductive receiver (defined as the receiver output current divided by the received terahertz power) is determined by the average photocurrent induced at the optimum phase adjustment between the optical pump and incident terahertz radiation.

The output noise current of the symmetrically pumped photoconductive receivers is determined by the photoconductor Johnson-Nyquist noise for a fully symmetric photoconductor. Accordingly, the root mean square value of the receiver output noise current is determined by the average photoconductor conductance:

$$i_{n-sym} = \sqrt{4k_B T \overline{G_p(t)} \Delta f} = \sqrt{\frac{4k_B T}{\left[\frac{hv.w_g^2}{\eta eq(\tau_n \mu_n + \tau_p \mu_p)P_0}\right]} \Delta f} \tag{14}$$

The tradeoff between the low-noise and high-responsivity operation of the symmetrically pumped photoconductive receivers can be analyzed by using Eqs. 13 and 14. While long-carrier lifetime photo-absorbing semiconductors offer higher receiver responsivity levels, short-carrier lifetime photo-absorbing semiconductors are more suitable for low-noise receiver operation. If the photoconductor exhibits an impedance larger than the antenna impedance ($R_A < 1/\overline{G_p(t)}$), which is the case of the heterodyne receiver shown in this work, the major portion of the induced terahertz voltage at the antenna terminal will appear across the photoconductor active region. In this state, reducing the gap between the photoconductor contact electrodes and increasing the optical pump power offer higher receiver responsivity levels but lead to higher receiver noise currents. On the other hand, if the photoconductor exhibits an impedance much smaller than the antenna impedance

$(R_A \gg 1/\overline{G_p(t)})$, a small portion of the induced terahertz voltage at the antenna terminal will appear across the photoconductor active region. In this state, reducing the gap between the photoconductor contact electrodes and increasing the optical pump power do not enhance the receiver responsivity, but increase the receiver output noise current.

### 3.2.2 Asymmetrically pumped terahertz receivers based on photoconductors

Similar analysis can be used to calculate the conductance and induced photocurrent of the asymmetrically pumped photoconductive receivers (Figure 7 (b)). If the pump photons have a uniform intensity within a distance $d_i$ from one of the photoconductor contact electrodes and are uniformly absorbed within the absorption depth, $1/\alpha$, photoconductor conductance can be determined by the conductance of the un-illuminated semiconductor area between the photoconductor contact electrodes, $G_{p\text{-}dark}$, and the conductance of the optically illuminated semiconductor area between the photoconductor contact electrodes, $G_{p\text{-}light}$,

$$G_p(t) = \left[\frac{1}{G_{p-light}(t)} + \frac{1}{G_{p-dark}}\right]^{-1} \tag{15}$$

where

$$G_{p-light}(t) = \frac{\eta_e q \tau_n \mu_n}{hv.d_i^2} P_0 \left[1 + \frac{P_\omega \sin(\omega t + \varphi_n(\omega))}{P_0 \sqrt{1+\omega^2 \tau_n^2}}\right] + \frac{\eta_e q \tau_p \mu_p}{hv.d_i^2} P_0 \left[1 + \frac{P_\omega \sin(\omega t + \varphi_p(\omega))}{P_0 \sqrt{1+\omega^2 \tau_p^2}}\right] \tag{16}$$

Using the equivalent circuit model of the photoconductive receiver, the induced photocurrent in the photoconductor can be calculated as

22

$$I_{p-asym}(t) = \begin{cases} \frac{\eta_e q \tau_n \mu_n}{hv.d_i.w_g} P_0 \left[1 + \frac{P_\omega \sin(\omega t + \varphi_n(\omega))}{P_0\sqrt{1+\omega^2\tau_n^2}}\right] \frac{V_{oc}\sin(\omega t + \varphi_0)}{1+(R_A+jX_A)\overline{(G_p(t)+j\omega C_p)}} & \sin(\omega t + \varphi_0) \geq 0 \\[4mm] \frac{\eta_e q \tau_p \mu_p}{hv.d_i.w_g} P_0 \left[1 + \frac{P_\omega \sin(\omega t + \varphi_p(\omega))}{P_0\sqrt{1+\omega^2\tau_p^2}}\right] \frac{V_{oc}\sin(\omega t + \varphi_0)}{1+(R_A+jX_A)\overline{(G_p(t)+j\omega C_p)}} & \sin(\omega t + \varphi_0) < 0 \end{cases}$$

$$(17)$$

Consequently, the photoconductor responsivity is determined by the average photocurrent induced at the optimum phase adjustment between the optical pump and incident terahertz radiation.

The output noise current of the asymmetrically pumped photoconductive receivers is determined by the photoconductor Johnson-Nyquist noise, as well as the photoconductor shot noise [79, 80]. The photoconductor shot noise cannot be neglected in this case, due to a non-zero diffusion photocurrent induced at the receiver output, in the absence of the incident terahertz radiation. The average diffusion photocurrent induced in the absence of the incident terahertz radiation can be calculated as

$$I_{diff} = \frac{q\eta_e}{hv.d_i} P_0 \left(\sqrt{\tau_n D_n} - \sqrt{\tau_p D_p}\right) \tag{18}$$

where $D_n = \mu_n kT/q$ and $D_p = \mu_p kT/q$ are electron and hole diffusion constants in the photo-absorbing semiconductor, respectively. Therefore, the RMS value of the receiver output noise current, calculated from the Johnson-Nyquist noise current, $i_{n\text{-}Nyquist}$, and shot noise current, $i_{n\text{-}shot}$, contributions, is given by

$$i_{n-asym} = \sqrt{\overline{i_{n-Nyquist}}^2 + \overline{i_{n-Shot}}^2} \tag{19}$$

where

$$i_{n-Nyquist} = \sqrt{4k_B T \overline{G_p(t)} \Delta f} = \sqrt{\frac{4k_B T}{\left[\frac{hv.d_i^2}{\eta_e q(\tau_n \mu_n + \tau_p \mu_p)P_0} + \frac{1}{G_{p-dark}}\right]}} \Delta f \qquad (20)$$

$$i_{n-Shot} = \sqrt{2q I_{diff} \Delta f} = \sqrt{\frac{2q^2 \eta_e}{hv.d_i} P_0 \left(\sqrt{\tau_n D_n} - \sqrt{\tau_p D_p}\right) \Delta f} \qquad (21)$$

The tradeoff between the low-noise and high-responsivity operation of the asymmetrically pumped photoconductive receivers can be analyzed using Eqs. 19, 20 and 21. Similar to the symmetrically pumped photoconductive receivers, long-carrier lifetime photo-absorbing semiconductors are more suitable for high-responsivity operation and short-carrier lifetime photo-absorbing semiconductors are more suitable for low-noise operation. The asymmetric illumination of the photoconductor active region helps maintaining an average photoconductor impedance much larger than the antenna impedance ($R_A \ll 1/\overline{G_p(t)}$). This enables the major portion of the induced terahertz voltage at the antenna terminal to appear across the photoconductor active region. Therefore, increasing the optical pump power enables enhancing the receiver responsivity, but leads to higher receiver output noise current. Moreover, reducing the gap between the photoconductor contact electrodes offers higher receiver responsivity levels without a negative impact on the receiver output noise current.

### 3.2.3 Comparisons of symmetrically and asymmetrically pumped terahertz receivers based on photoconductors

In order to compare the performance of the symmetrically pumped and asymmetrically pumped photoconductive terahertz receiver architectures, photoconductive terahertz receivers based on GaAs and InGaAs substrates are analyzed. GaAs and InGaAs are the most commonly used photo-absorbing substrates for operation at near-infrared and telecommunication optical pump

wavelengths, respectively. While a long-carrier lifetime photo-absorbing semiconductor can be used for both pulsed and continuous-wave device operation, short-carrier lifetime photo-absorbing semiconductors are usually required for continuous-wave device operation to prevent any undesired destructive interferences in the output of the receiver. In order to evaluate the impact of the carrier lifetime on the receiver performance, semi-insulating GaAs (SI-GaAs) and un-doped InGaAs are considered as photo-absorbing semiconductors with long-carrier lifetime and low-temperature grown GaAs (LT-GaAs) and ErAs-doped InGaAs (ErAs:InGaAs) are considered as photo-absorbing semiconductors with short-carrier lifetime. The physical parameters of the semiconductors employed in this analysis are listed in Table 1.

| Substrate | $\tau$ [s] | $\mu_n$[cm$^2$/(V·s)] | $\mu_p$ [cm$^2$/(V·s)] | $\rho$ [Ω·cm)] |
|---|---|---|---|---|
| SI-GaAs [74] | $1.2\times10^{-9}$ | 5600 | 350 | $5.2\times10^7$ |
| LT-GaAs [78] | $2\times10^{-13}$ | 200 | 12.5 | $10^7$ |
| Un-doped InGaAs [75, 77] | $3.1\times10^{-7}$ | 11000 | 250 | 0.025 |
| ErAs:InGaAs [76] | $2\times10^{-13}$ | 490 | 19.6 | 340 |

Table 1. Carrier lifetime ($\tau$), electron mobility ($\mu_n$), hole mobility ($\mu_p$), and substrate resistivity ($\rho$), of the photo-absorbing semiconductors used for comparing the performance of symmetrically pumped and asymmetrically pumped photoconductive terahertz receivers [74 - 78]. We assume a 500 μm-thick SI-GaAs substrate and 1 μm-thick LT-GaAs, un-doped InGaAs, and ErAs:InGaAs layers grown on lattice-matched substrates.

The responsivity and output noise current of the symmetrically pumped and asymmetrically pumped photoconductive terahertz receivers based on the listed photo-absorbing photoconductors are calculated as a function of the optical pump power and device geometry. An antenna radiation resistance of $R_A = 70\ \Omega$ and a photoconductor active region width of $w_e = 10\ \mu m$ are assumed for the calculations. While a uniform optical pump illumination is considered for the entire

photoconductor active region of the symmetrically pumped receivers, an optical pump spot size of $d_i = 5\ \mu m$ is assumed for the asymmetrically pumped receivers.



Figure 8. Responsivity of the symmetrically pumped and asymmetrically pumped photoconductive terahertz receivers based on (a) SI-GaAs, (b) LT-GaAs, (c) un-doped InGaAs, and (d) ErAs:InGaAs photo-absorbing substrates at 1 THz.

Figure 8 shows the responsivity of the symmetrically pumped and asymmetrically pumped photoconductive receivers at 1 THz. At the same optical pump power and for the same photoconductor geometry, the asymmetrically pumped photoconductive receivers offer higher responsivity levels compared to the symmetrically pumped photoconductive receivers. This is because of the higher concentration of the photo-generated carriers near the photoconductor contact electrode in the asymmetric receiver architecture. A straightforward way to increase the

photocarrier concentration near the contact electrodes of the symmetrically pumped photoconductive receivers is employing smaller semiconductor gap between photoconductor contact electrodes. However, as we will explain in the next section, smaller semiconductor gap between photoconductor contact electrodes could lead to higher output noise currents in symmetrically pumped photoconductive receivers.

Another advantage of the asymmetrically pumped photoconductive receiver architecture is that it makes it easy to maintain high photoconductor impedance levels, even at high optical pump power levels. This allows increasing receiver responsivity at high optical pump power levels and achieving large receiver dynamic ranges. As illustrated in Figure 8 (a) and 8 (c), the symmetrically pumped photoconductive receivers based on SI-GaAs and un-doped InGaAs do not offer large dynamic ranges. This is because of the dramatic reduction in the photoconductor impedance when illuminating the entire semiconductor gap between the photoconductor contact electrodes, reducing the induced terahertz voltage across the photoconductor active region. Therefore, although photocarrier concentration levels increase at higher optical pump power levels, the severe reduction in the induced terahertz voltage across the photoconductor active region prevents achieving high responsivity levels at high optical pump powers.
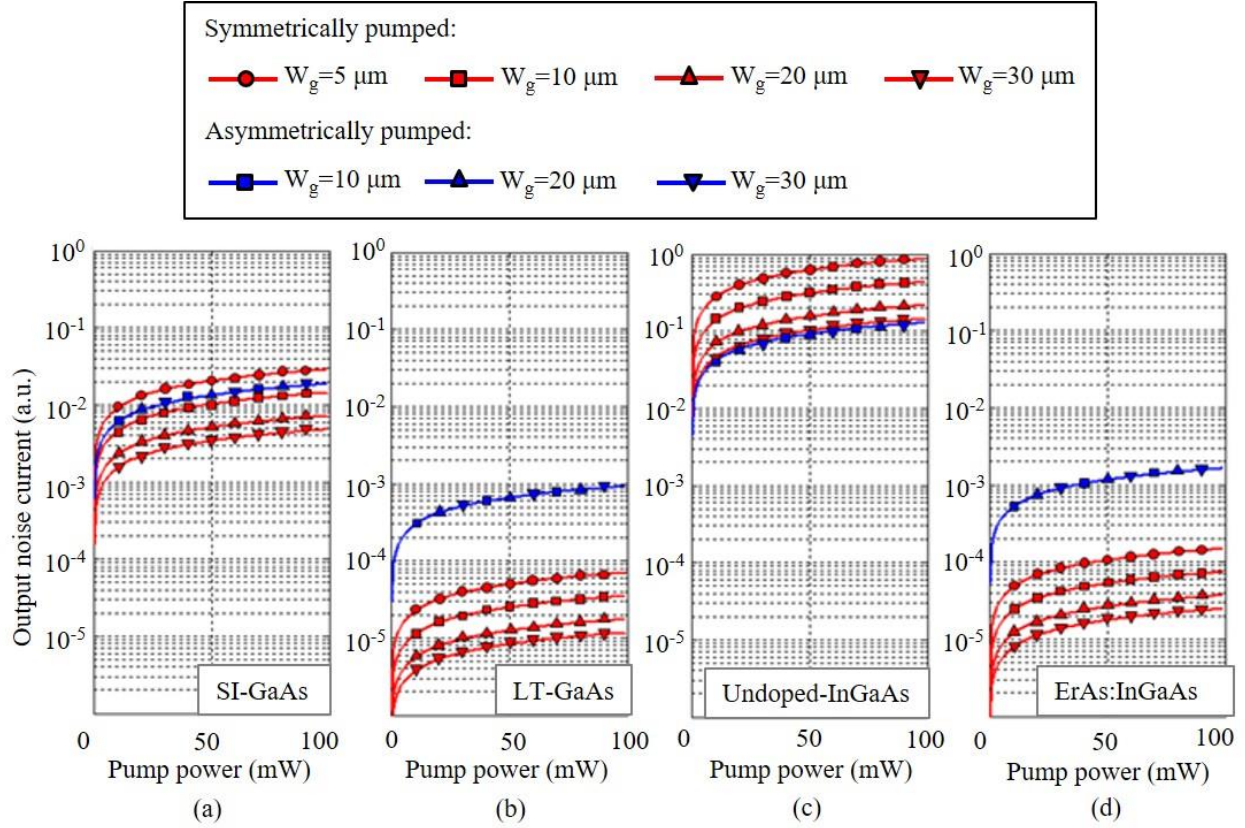
Figure 9. Output noise current of the symmetrically pumped and asymmetrically pumped photoconductive terahertz receivers based on (a) SI-GaAs, (b) LT-GaAs, (c) un-doped InGaAs, and (d) ErAs:InGaAs photo-absorbing substrates at 1 THz.

Figure 9 shows the output noise current of the symmetrically pumped and asymmetrically pumped photoconductive receivers at 1 THz. The Johnson-Nyquist noise and shot noise are the dominant noise sources for the symmetrically pumped and asymmetrically pumped photoconductive receivers, respectively. Therefore, while reducing the semiconductor gap between the photoconductor contact electrodes increases the output noise current of the symmetrically pumped photoconductive receivers, it does not have any negative impact on the noise performance of the asymmetrically pumped photoconductive receivers. Moreover, independent of the photoconductive receiver architecture, short-carrier lifetime semiconductors offer lower output

noise currents compared to long-carrier lifetime semiconductors. This is because of the higher impedance levels and lower DC responsivity levels of the photoconductors based on short-carrier lifetime semiconductors.
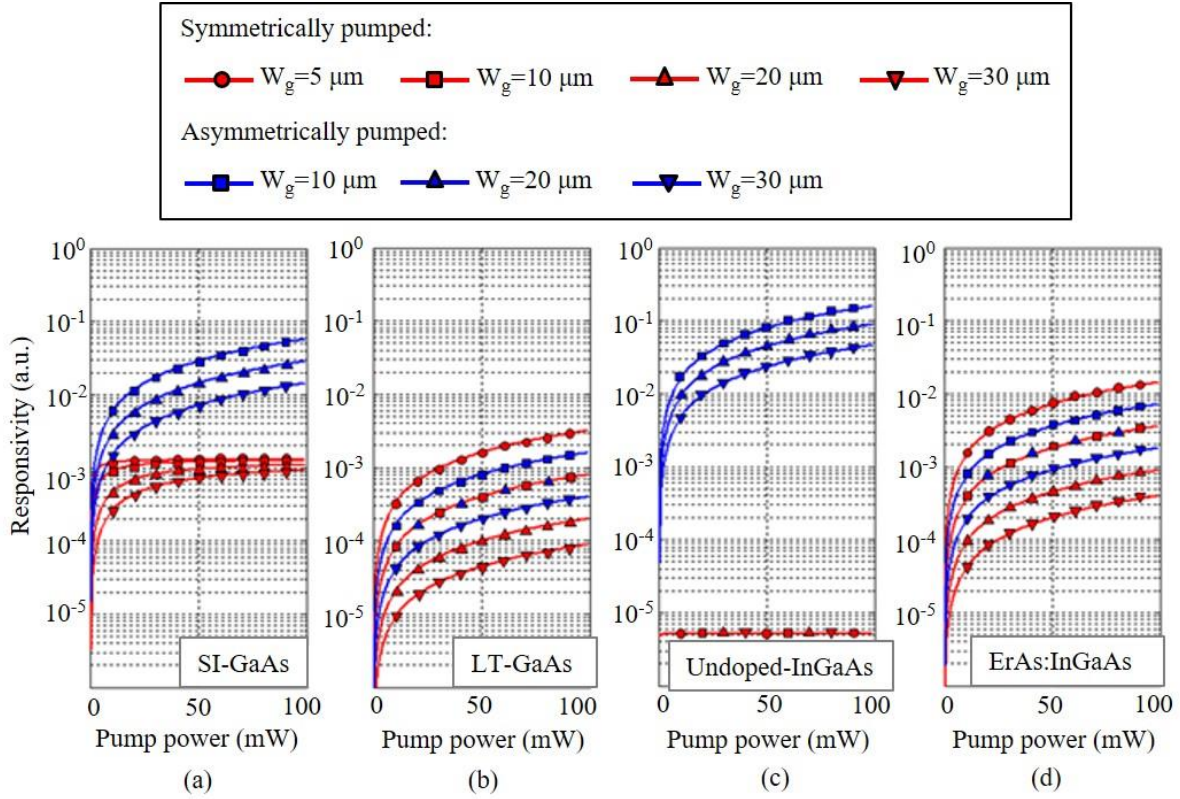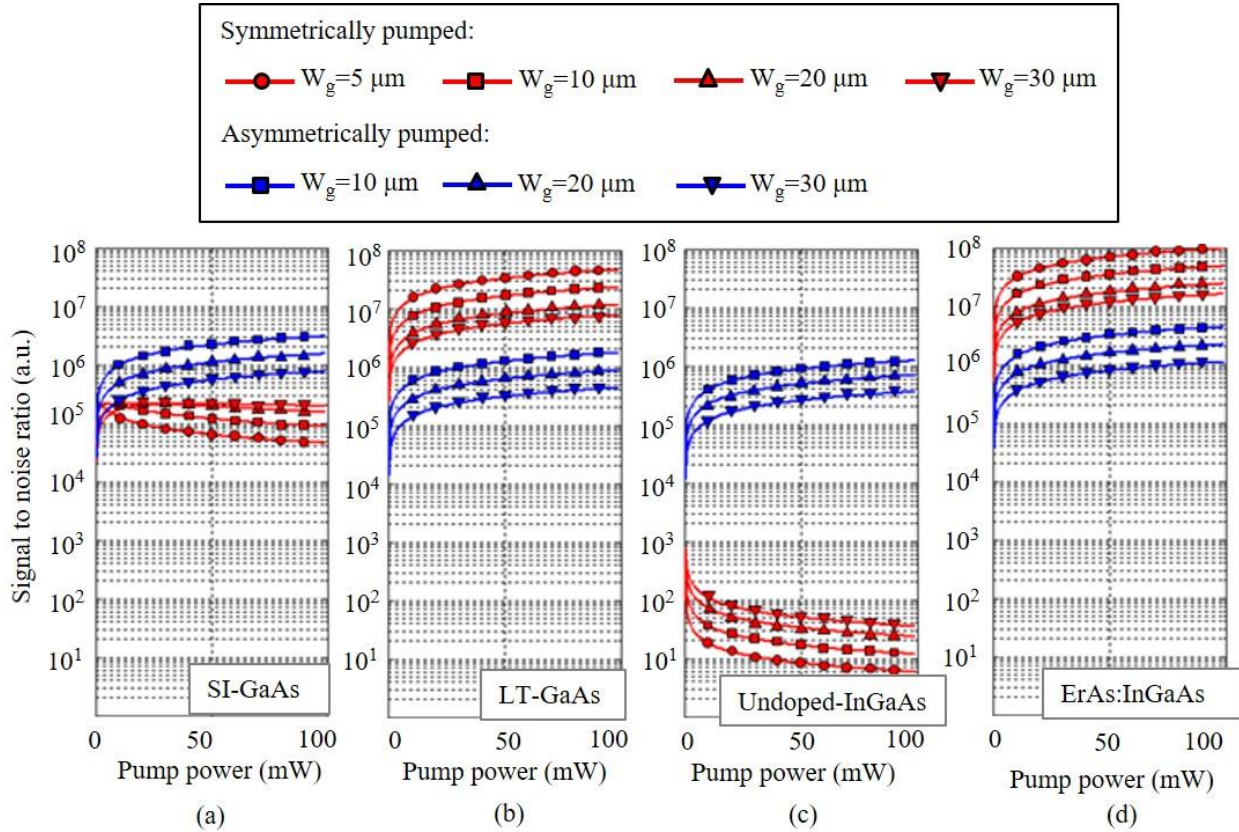


Figure 10. Relative signal-to-noise ratio of the symmetrically pumped and asymmetrically pumped photoconductive terahertz receivers based on (a) SI-GaAs, (b) LT-GaAs, (c) un-doped InGaAs, and (d) ErAs:InGaAs photo-absorbing substrates at 1 THz.

The signal-to-noise ratio of the symmetrically pumped and asymmetrically pumped photoconductive receivers is calculated using the responsivity and noise data. Figure 10 shows the signal-to-noise ratio of the symmetrically pumped and asymmetrically pumped photoconductive receivers at 1 THz. The results indicate that the symmetrically pumped photoconductive receiver architecture offers higher signal-to-noise ratios for the photoconductive receivers based on short-

carrier lifetime semiconductors due to their superior noise performance. The results also indicate that the asymmetrically pumped photoconductive receiver architecture offers higher signal-to-noise ratios for the photoconductive receivers based on long-carrier lifetime semiconductors due to their superior responsivity performance. If the photoconductor exhibits an impedance level much smaller than the antenna radiation resistance (e.g. the symmetrically pumped photoconductive receivers based on SI-GaAs and un-doped InGaAs), increasing the optical pump power leads to lower signal-to-noise ratios. Otherwise, higher signal-to-noise ratios are achieved at higher optical pump power levels.

## 3.3   Conclusion

In conclusion, we have analyzed the performance of the photoconductive terahertz receivers with symmetrically pumped and asymmetrically pumped receiver architectures and investigated the responsivity and noise performance of each receiver architecture as a function of various device parameters and operational settings. Our analysis shows that increasing the optical pump power does not necessarily offer higher signal-to-noise ratios and its impact is determined by the photoconductive receiver architecture, geometry and the photo-absorbing semiconductor. Moreover, our analysis indicates that the highest signal-to-noise ratios are offered by the symmetrically pumped and asymmetrically pumped receiver architectures for the photoconductive receivers based on short-carrier lifetime and long-carrier lifetime semiconductors, respectively.

# CHAPTER 4

# High Sensitivity Photoconductive Terahertz Receivers based on Plasmonic Contact Electrodes

Photoconductive terahertz receivers are extensively used in time-domain and frequency-domain terahertz imaging and spectroscopy systems for various applications, such as chemical sensing, product quality control, medical imaging, bio-sensing, pharmaceutical analysis, and security screening, etc. A photoconductive terahertz receiver consists of an ultrafast photoconductor pumped by a pulsed optical pump. The ultrafast photoconductor is integrated with a terahertz antenna, which receives incident terahertz radiation and induces a terahertz electric field across the photoconductor contact electrodes. Terahertz detection is the result of the induced terahertz field drifting photo-generated carriers inside the photoconductor active region, generating an output photocurrent proportional to the intensity of the incident terahertz field. The inherent tradeoff between high quantum efficiency and ultrafast operation of conventional photoconductors has severely limited the detection sensitivity of conventional photoconductive terahertz receivers. To address the quantum efficiency limitation of ultrafast photoconductors, we present a new type of photoconductive receiver that enables high quantum efficiency and ultrafast operation, simultaneously. This new type of photoconductive receiver incorporates plasmonic contact electrodes to manipulate the distribution of the photo-generated carriers inside the photoconductor

active region and enhance carrier concentration in close proximity with photoconductor contact electrodes. By reducing the carrier transport path to the photoconductor contact electrodes, the number of the drifted carriers to the photoconductor contact electrodes within a sub-picosecond time-scale is increased significantly, offering higher detection sensitivities of the incident terahertz radiation. We also experimentally demonstrate that incorporating plasmonic gratings in the contact electrodes of a conventional photoconductive terahertz receiver offers a 30 fold enhancement in the terahertz detection sensitivity over 0.1-1.5 THz frequency range.

## 4.1 Design of Photoconductive Terahertz Receiver based on Plasmonic Contact Electrodes

To evaluate the impact of plasmonic contact electrodes in enhancing the detection sensitivity of photoconductive terahertz receivers, we have characterized the performance of a conventional photoconductive terahertz receiver before and after incorporating plasmonic contact electrodes.

Figure 11 (a) shows the schematic diagram and operation concept of the conventional photoconductive terahertz receiver used in this study. The receiver consists of an ultrafast photoconductor with 30 μm contact electrode width and 10 μm contact electrode spacing. The ultrafast photoconductor is integrated with a 60 μm long bowtie antenna with maximum and minimum widths of 100 μm and 30 μm, respectively, on a low-temperature grown GaAs substrate. The receiver is mounted on a silicon lens, which helps focusing the incident terahertz radiation onto the device. When a terahertz beam is incident on the receiver, a terahertz electric field, $E_{THz}$, is induced across photoconductor contact electrodes, which drifts the photocarriers generated upon incidence of an optical pump. This generates an output photocurrent, $I_{out}$, which follows the envelope of the received terahertz field. For high sensitivity terahertz detection, the optical pump

is focused onto the photoconductive gap asymmetrically close to one of the photoconductor contact electrodes. Asymmetric optical excitation enhances the photocarrier concentration in close proximity to the photoconductor contact electrode with the highest induced terahertz electric field levels and, thus, the output photocurrent. However, due to the relatively low drift velocity of carriers in the photo-absorbing substrate, a small portion of the photocarriers can reach the photoconductor contact electrodes within a sub-picosecond time-scale, limiting the terahertz detection sensitivity of the conventional photoconductive terahertz receiver.



(a)                                    (b)
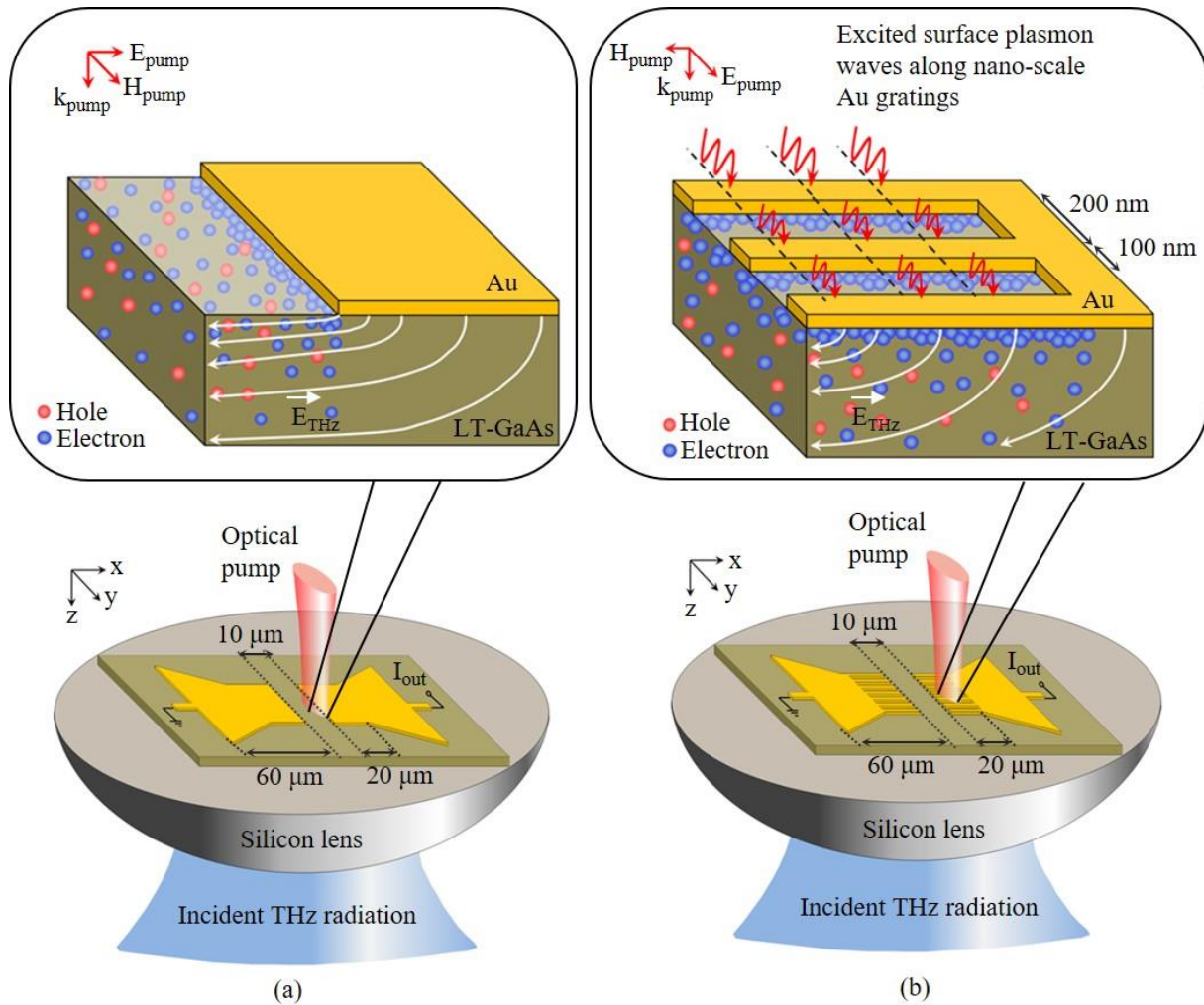
Figure 11. Schematic view and operation concept of comparable (a) conventional and (b) plasmonic photoconductive terahertz receivers, used for evaluating the impact of plasmonic contact electrodes on the photoconductive terahertz receiver performance.

Figure 11 (b) shows the schematic diagram and operation concept of the plasmonic photoconductive terahertz receiver, designed to increase the detection sensitivity of the conventional photoconductive terahertz receiver, by incorporating plasmonic gratings in the photoconductor contact electrodes. The plasmonic contact electrode gratings (200 nm pitch, 100 nm spacing, and 45 nm thick Au and 5 nm Ti gratings in this case) are designed to allow excitation of surface plasmon waves along the nanoscale gratings in response to a TM-polarized incident optical pump at 800 nm wavelength. Excitation of the surface plasmon waves enables transmission of more than 70% of the optical pump into the nanoscale semiconductor active regions between the plasmonic contact electrode gratings, as illustrated in Figure 12 (a). Moreover, since the excited surface plasmon waves are tightly confined at the metal-semiconductor interface, the optical pump intensity is further enhanced in close proximity to the Au contact electrodes, as illustrated in Figure 12 (b). Therefore, the average transport path of the photo-generated carriers to the photoconductor contact electrodes is significantly reduced compared to the case of the conventional photoconductive terahertz receiver, leading to a significant increase in the number of the drifted carriers to the photoconductor contact electrodes in a sub-picosecond time-scale. Therefore, while the output photocurrents of the plasmonic and conventional photoconductive receivers both follow the envelope of the received terahertz field, significantly larger output photocurrents will be offered by the plasmonic photoconductive detector under the same incident terahertz intensities.

An additional advantage of the presented plasmonic photoconductive receiver in comparison with conventional photoconductive receivers is that the device active area can be increased by extending

the length of the plasmonic contact electrodes, without a considerable increase in photoconductor capacitive parasitics. Increasing the photoconductor active area enables mitigating the carrier screening effect and optical breakdown at high optical pump power levels. Therefore, this design flexibility is helpful to enhance the highest achievable detection responsivity and sensitivity by increasing the optical pump power.
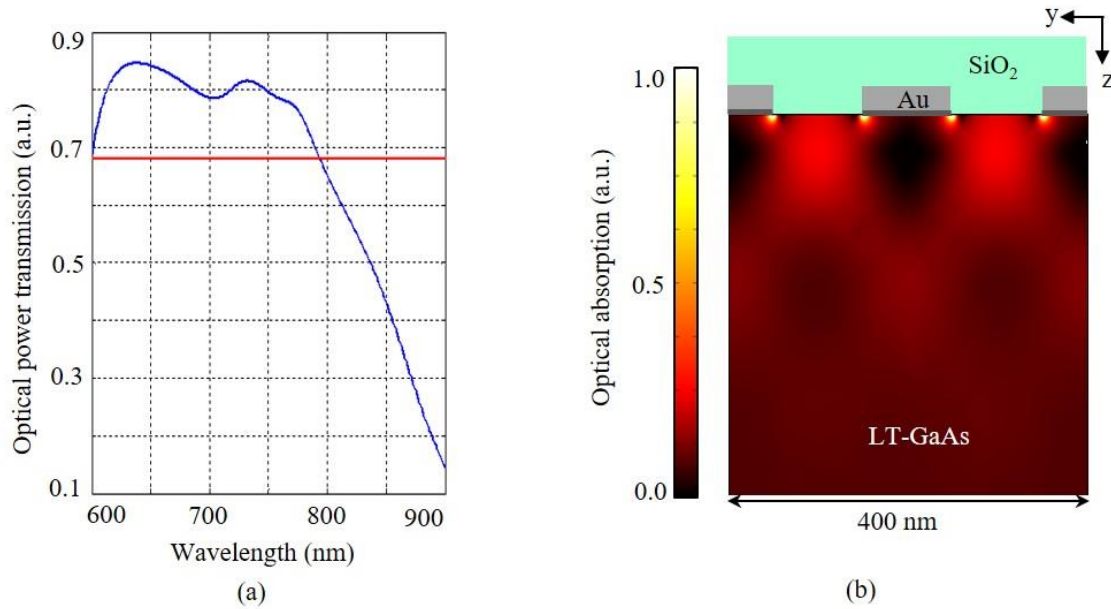


Figure 12. Optical power transmission and carrier concentration of the designed plasmonic gratings, simulated in COMSOL simulator. (a) Optical power transmission through the designed plasmonic contact electrodes with 200 nm pitch, 100 nm spacing, 45 nm thick Au and 5 nm thick Ti gratings, and 150 nm SiO2 passivation layer into the active region of the plasmonic photoconductive receiver (blue curve) and its comparison with optical power transmission into the active region of the conventional photoconductive receiver (red curve). (b) Absorption of a 800 nm optical pump (y-polarized) inside the LT-GaAs substrate at the plasmonic contact electrodes cross section, indicating optical absorption enhancement in close proximity with the plasmonic contact electrodes.

## 4.2 Photoconductive Terahertz Receiver Prototypes Fabrication

35

Prototypes of comparable conventional and plasmonic photoconductive terahertz receivers (Figure 13) were fabricated on the same LT-GaAs substrate. Using electron beam lithography, the plasmonic gratings were first patterned, followed by deposition of Ti/Au (50/450 Å) and liftoff. A 1500 Å SiO$_2$ passivation layer was then deposited using plasma enhanced chemical vapor deposition. Using optical photolithography and dry plasma etching, contact vias were etched through the SiO$_2$ layer. Finally, the antennas, bias lines, and vias were patterned using optical lithography, followed by Ti/Au (100/4000 Å) deposition and liftoff. Figure 13 shows the microscope image of the conventional and plasmonic photoconductive receiver prototypes as well as the scanning electron microscope (SEM) image of the plasmonic contact electrode gratings of the plasmonic photoconductive receiver prototype. The conventional and plasmonic photoconductive terahertz receiver prototypes were then mounted on the same silicon lens and characterized under the same operation conditions.



Figure 13. Microscope image of the fabricated (a) conventional and (b) plasmonic photoconductive receivers, as well as the SEM image of the plasmonic contact electrode gratings incorporated in the plasmonic photoconductive receiver.
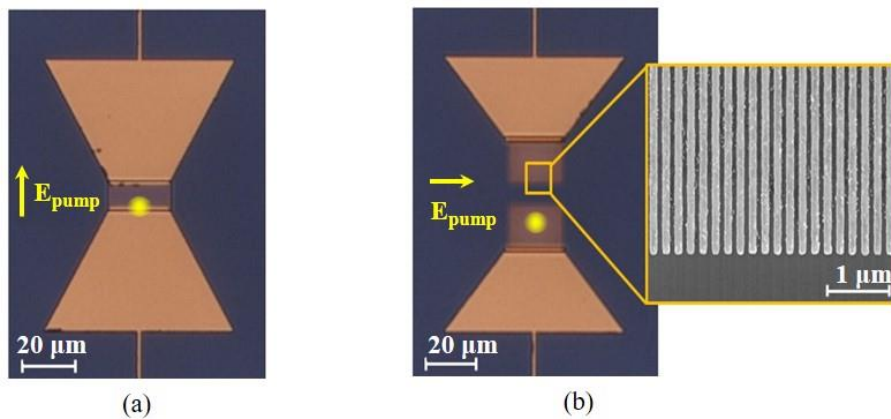
## 4.3 Experimental Results and Discussions

The performance of the conventional and plasmonic photoconductive receiver prototypes in response to an incident radiation from a commercially available photoconductive terahertz emitter (iPCA-21-05-1999-800-h) was characterized in a time-domain terahertz spectroscopy setup (Figure 14). A Ti: Sapphire mode-locked laser with 200 fs pulses at 800 nm wavelength and 76 MHz repetition rate was used for pumping the photoconductive terahertz emitter and the photoconductive terahertz receiver prototypes at the same time. First, the beam from the Ti: Sapphire mode-locked laser was split into a pump beam and a probe beam. Next, the pump and probe beams were focused onto the photoconductive terahertz emitter and receiver prototypes, respectively. The emitted radiation from the photoconductive terahertz emitter was modulated by controlling bias voltage of the terahertz emitter, and subsequently focused onto the photoconductive terahertz receiver prototypes by using two polyethylene spherical lenses. Finally, the output current of the photoconductive terahertz receiver prototypes was measured by a lock-in amplifier with the terahertz radiation modulation reference. By inserting a controllable optical delay line in the optical pump path, the time delay between the optical probe and terahertz pulses was varied, and the time-domain output photocurrent of the photoconductive terahertz receiver prototypes was measured accordingly. To achieve the highest output photocurrent levels from the photoconductive receiver prototypes, the optical pump spot was focused asymmetrically onto the photoconductive gap and the optical pump polarization was set along the x-axis and y-axis for the conventional and plasmonic photoconductive receivers, respectively. Each measurement was repeated for various optical pump spot positions along the photoconductive gap until the highest output photocurrent level was achieved for each receiver prototype.
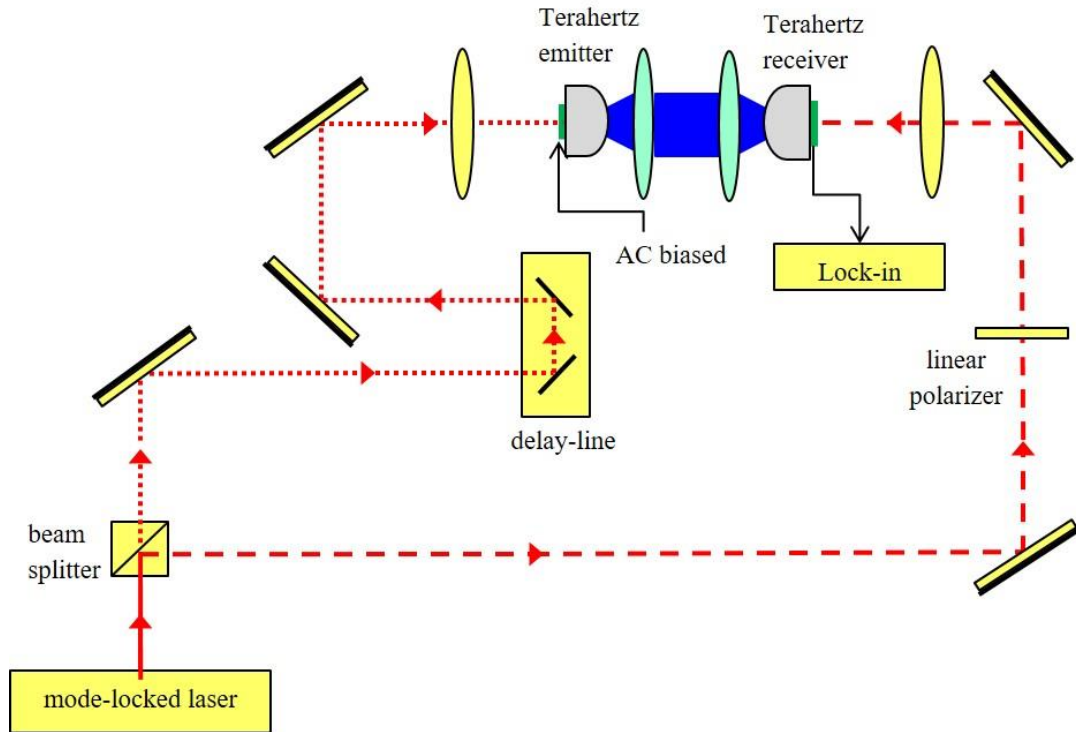
Figure 14. Time-domain spectroscopy setup to characterize the conventional and plasmonic photoconductive terahertz receiver prototypes.

The measured time-domain output photocurrent of the conventional and plasmonic photoconductive terahertz receivers, pumped by a 50 mW optical beam, is shown in Figure 15 (a). While the output photocurrent of both photoconductive terahertz receivers follow the envelope of the received electric field from the photoconductive terahertz emitter used in the terahertz spectroscopy setup, 30 times higher output photocurrent levels are achieved by using the plasmonic photoconductive terahertz receiver. The frequency-domain output photocurrent of the photoconductive terahertz receiver prototypes, obtained by calculating the Fourier transform of the measured time-domain output photocurrents, is shown in Figure 15 (b). The calculated output photocurrent spectra indicate that the 30 fold output photocurrent enhancement offered by the plasmonic photoconductive terahertz receiver is maintained over 0.1-1.5 THz frequency range.
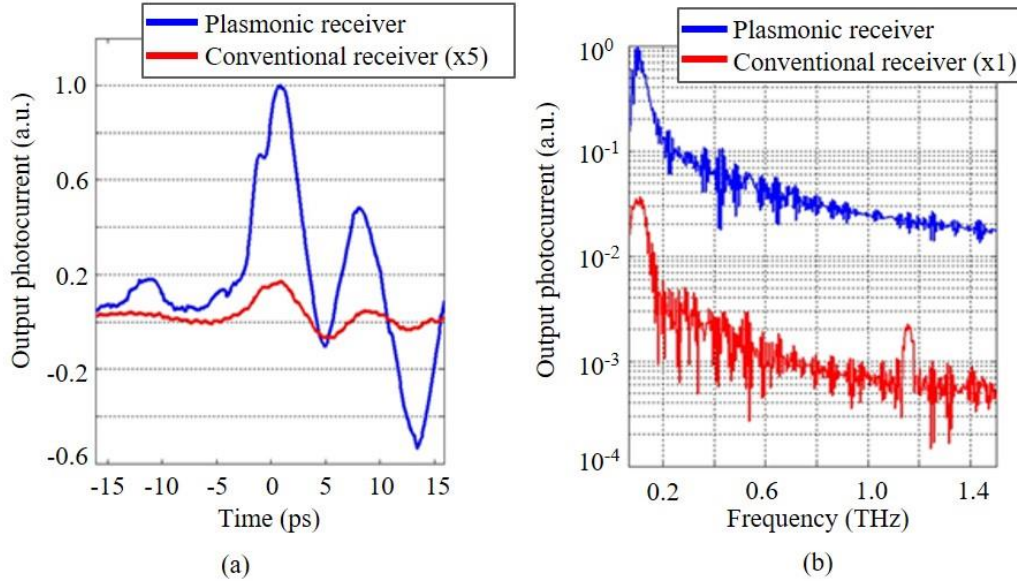
Figure 15. Measured output photocurrent of the conventional and plasmonic photoconductive receiver prototypes in the (a) time-domain and (b) frequency-domain.

To compare the terahertz detection sensitivity of the conventional and plasmonic photoconductive receiver prototypes, their output current noise levels were evaluated. The output current noise of each photoconductive receiver prototype was calculated by measuring its output photocurrent spectra in the time-domain terahertz spectroscopy setup, while blocking the incident terahertz radiation from the photoconductive terahertz emitter. Figure 16 (a) shows the output current noise of the conventional and plasmonic photoconductive receiver prototypes at a 50 mW optical pump power, indicating similar output current noise spectra for the conventional and plasmonic photoconductive receiver prototypes. The same output noise level for the conventional and plasmonic photoconductive receiver prototypes is due to the dominance of the Johnson–Nyquist noise rather than the photoconductor Shot noise in both photoconductive receiver prototypes.

39
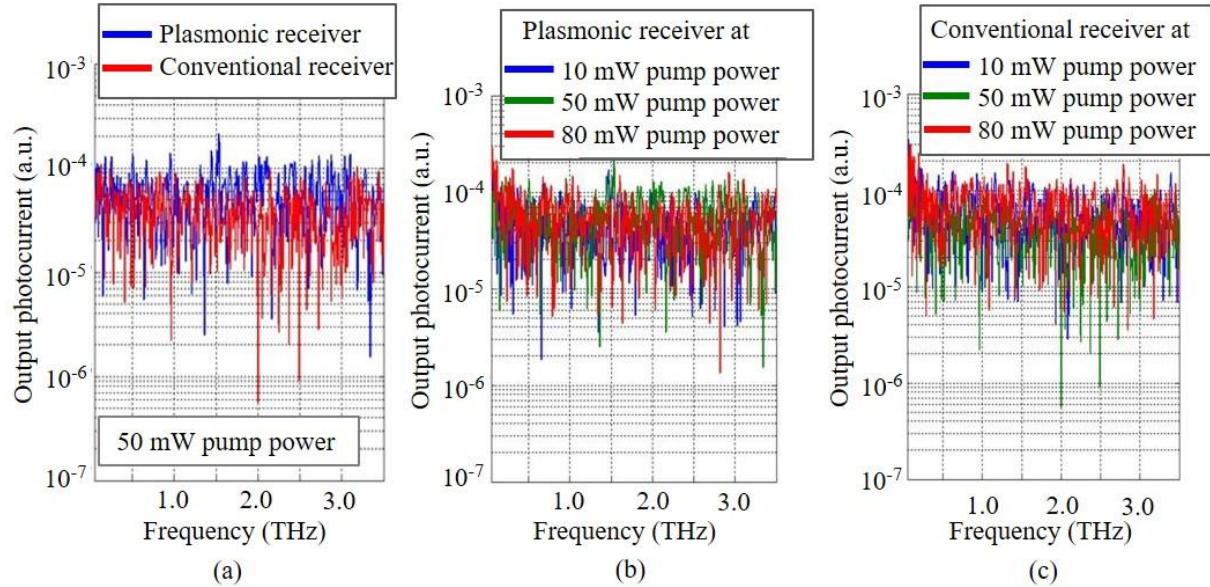
Figure 16. Output current noise evaluations for conventional and plasmonic photoconductive terahertz receiver prototypes. (a) The output current noise of the conventional and plasmonic photoconductive receiver prototypes at 50 mW optical pump power, (b) The output noise level of the plasmonic photoconductive receiver and (c) the conventional photoconductive receiver at various optical pump power levels ranging from 10 mW to 80 mW.

To further evaluate this hypothesis, the output current noise of the plasmonic and conventional photoconductive receivers were measured at various optical pump power levels ranging from 10 mW to 80 mW, as shown in Figure 16 (b) and Figure 16 (c). The measured output noise levels of the plasmonic and conventional photoconductive receiver prototypes show no dependence on the optical pump power levels over the 10 − 80 mW pump power range, validating the dominance of the Johnson–Nyquist noise (rather than photoconductor Shot noise) in the device operation regime. Since both photoconductive receiver prototypes have the same output current noise levels, the 30 fold responsivity enhancement offered by the plasmonic photoconductive receiver enables achieving 30 times higher detection sensitivities over the 0.1-1.5 THz frequency band.

## 4.4  Conclusion

In conclusion, a photoconductive terahertz receiver based on nanoscale plasmonic contact electrode gratings is presented and experimentally demonstrated. The presented plasmonic photoconductive receiver addresses the quantum efficiency limitation of ultrafast photoconductors by significantly enhancing the concentration of the photo-generated carriers in close distances from photoconductor contact electrodes. Experimental results demonstrate that more than 30 times higher terahertz detection sensitivities can be achieved by a plasmonic photoconductive terahertz receiver compared to comparable photoconductive terahertz receivers without plasmonic contact electrodes over 0.1-1.5 THz. The terahertz detection sensitivity enhancement offered by plasmonic photoconductive receivers in combination with the terahertz radiation power enhancement offered by plasmonic photoconductive emitters would have a significant impact on future time-domain and frequency-domain terahertz imaging and spectroscopy systems by offering substantially higher signal-to-noise ratio levels.

# CHAPTER 5

# High Sensitivity Heterodyne Terahertz Receivers based on Plasmonic Photomixers

Heterodyne terahertz receivers have extensive usage in communication, sensing and imaging applications due to their high spectral resolution and high sensitivity [34, 101 - 102]. A conventional heterodyne terahertz receiver consists of a terahertz mixer that mixes a received terahertz signal at $f_{THz}$ with a local oscillator signal at $f_{LO}$ to generate an intermediate frequency (IF) signal at $|f_{THz} – f_{LO}|$ (Figure 17 (a)). By an appropriate choice of the local oscillator frequency, the IF signal falls in the RF frequency range, where it can be easily processed and detected by RF electronics. Schottky diode mixers, superconductor-insulator-superconductor (SIS) mixers and hot electron bolometer (HEB) mixers are the most commonly used mixers in conventional heterodyne terahertz receivers [34]. While conventional heterodyne terahertz receivers offer high spectral resolution and high detection sensitivity levels at cryogenic temperatures, their operation bandwidth and room-temperature sensitivity is limited by narrow frequency tunability and low radiation power of terahertz local oscillators. To address this limitation, we present a new heterodyne terahertz detection scheme based on plasmonic photomixing (Figure 17 (b)). The presented design replaces terahertz mixer and local oscillator of conventional heterodyne terahertz receivers with a plasmonic photomixer pumped by an optical local oscillator. The optical local

oscillator consists of two wavelength-tunable continuous-wave optical lasers with a terahertz frequency difference. As a result, the detection bandwidth and sensitivity of the presented heterodyne receiver is not limited by radiation frequency and power restrictions of conventional terahertz sources.
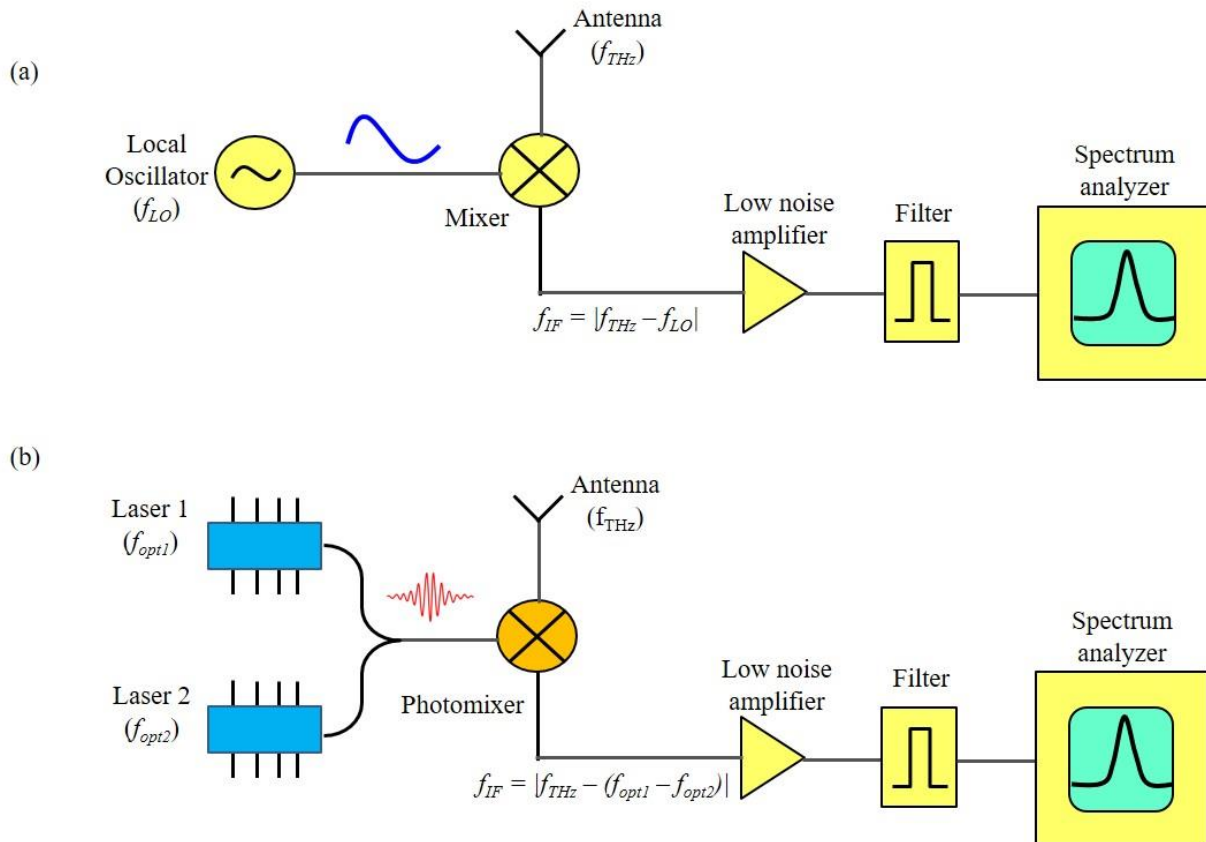


Figure 17. Block diagram of (a) conventional heterodyne terahertz receivers and (b) heterodyne terahertz receivers based on plasmonic photomixers.

In this chapter, different designs of heterodyne terahertz receivers based on plasmonic photomixers will be discussed. Different terahertz receiver prototypes are designed, fabricated, and characterized. The experimental results indicate the unique capabilities of the new heterodyne receiver concept in offering large dynamic ranges and broad operation bandwidths at room temperature.

## 5.1 First Generation Heterodyne Terahertz Receiver based on a Plasmonic Photomixer with a Dipole Antenna

As the first proof of concept prototype, a heterodyne terahertz receiver based on a plasmonic photomixer integrated with a dipole antenna is designed, fabricated and characterized. This is our first generation heterodyne terahertz receiver based on a plasmonic photomixer.

### 5.1.1 Design of the first generation heterodyne terahertz receiver based on a plasmonic photomixer with a dipole antenna
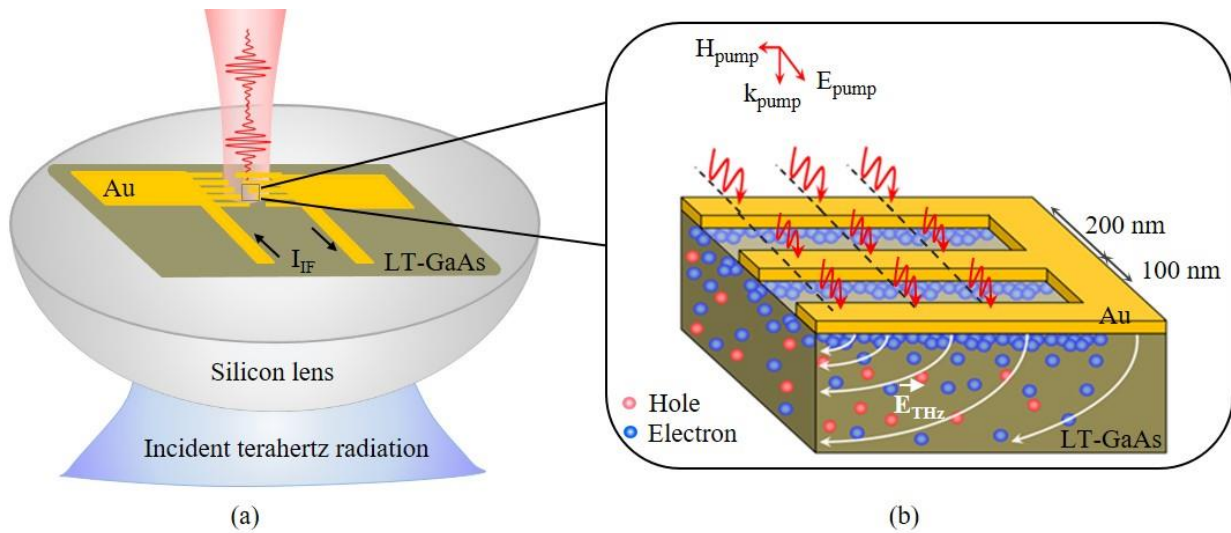


Figure 18. Schematic diagram and operation concept of the heterodyne terahertz receiver based on plasmonic photomixing.

Figure 18 shows the schematic diagram and operation concept of the first generation heterodyne terahertz receiver. It consists of a plasmonic photomixer fabricated on a photo-absorbing substrate, pumped by an optical local oscillator. The optical local oscillator is provided by two continuous-wave optical sources at $f_{opt1}$ and $f_{opt2}$ frequencies. Therefore, the concentration of photo-generated carriers, which follows the intensity envelope of the optical pump beam, has a sinusoidal temporal

variation with $|f_{opt1} - f_{opt2}|$ frequency. The photomixer is integrated with a terahertz antenna such that an incident terahertz beam induces a terahertz electric field across the photomixer plasmonic contact electrodes, drifting the photo-generated carriers. The resulting photocurrent, which consists of both diffusion and drift photocurrent components, contains an IF output at frequency $|f_{THz} - |f_{opt1} - f_{opt2}||$. By an appropriate choice of the optical frequencies, the IF output falls in the RF frequency range. Therefore, the intensity and spectral information of the incident terahertz radiation are determined by measuring the intensity and spectral information of the IF output.
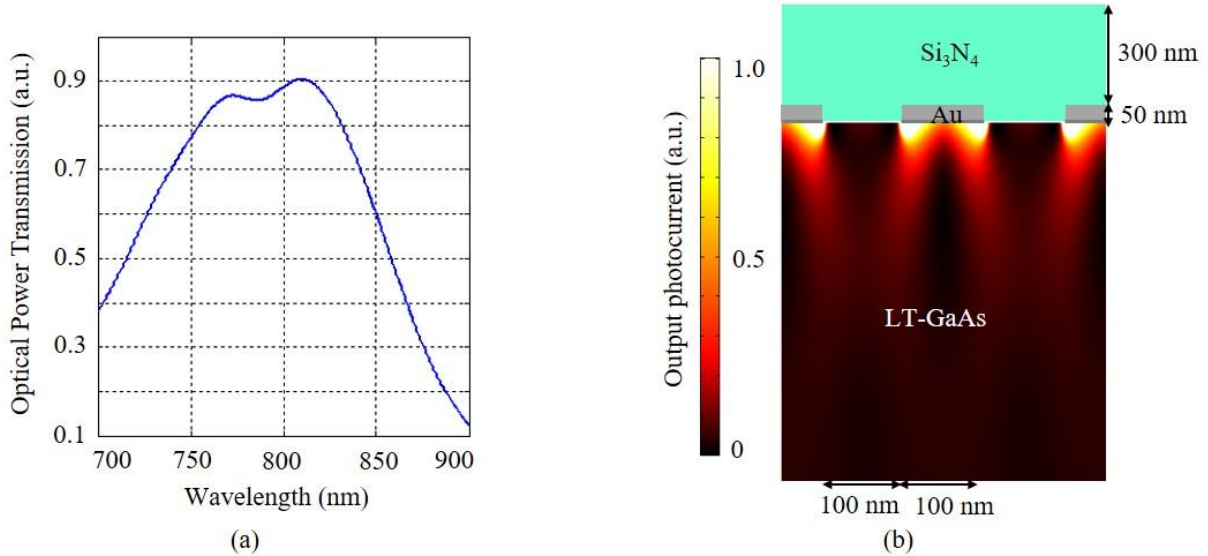


Figure 19. Finite-element (COMSOL) simulation results of (a) optical power transmission through the plasmonic electrodes at different wavelengths, (b) optical pump power absorption inside the photo-absorbing substrate.

A proof-of-concept heterodyne receiver is designed for operation at 0.1 THz frequency range. Plasmonic gold gratings (200 nm pitch, 100 nm spacing, and 50 nm height) with a 300 nm thick of silicon nitride anti-reflection coating are used as the photomixer plasmonic contact electrodes. This allows transmission of ~85% of a TM-polarized optical pump beam at ~784 nm wavelength through the plasmonic contact electrodes into the LT-GaAs substrate (Figure 19). Since optical

45

transmission through the plasmonic gratings is accompanied by excitation of surface plasmon waves, a large fraction of the photo-generated carriers is concentrated in close proximity to the contact electrode [86 - 87]. By reducing the average transport path distance of the photo-generated carriers to the contact electrodes, high quantum efficiencies and terahertz-to-IF conversion efficiencies are achieved.
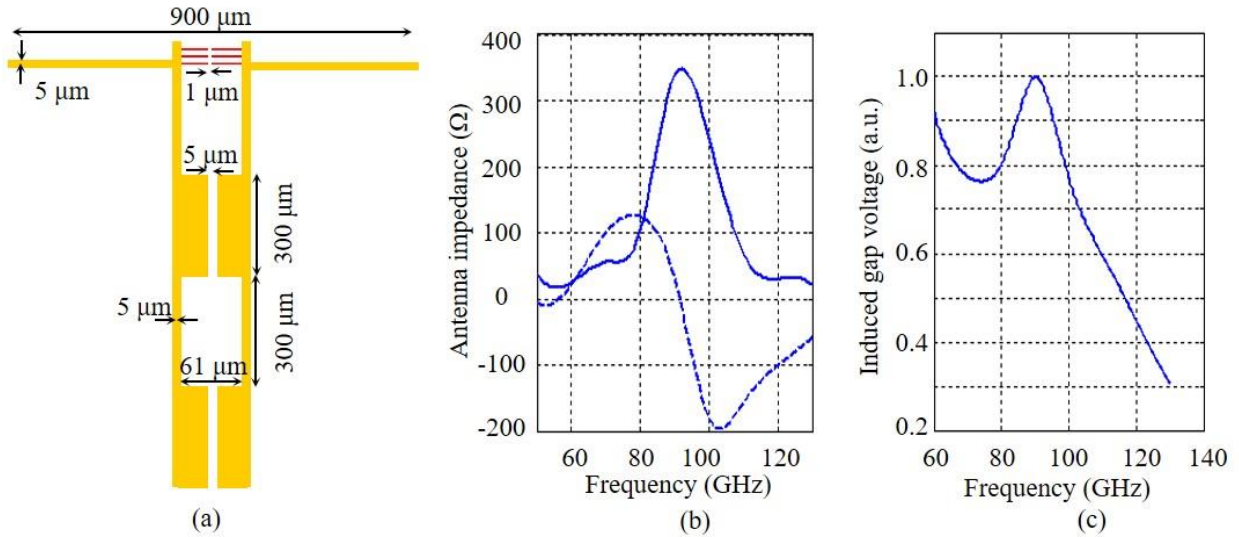


Figure 20. Terahertz dipole antenna design using HFSS simulations. (a) The full-wavelength dipole antenna integrated with the plasmonic grating electrodes and an IF transmission line with a terahertz choke. (b) Real (solid curve) and imaginary (dashed line) parts of the antenna impedance. (c) Induced voltage at the input port of the antenna between the anode and cathode gratings. The incident radiation has a linear polarization along the dipole arms and is incident from the back side of the substrate.

A full-wavelength dipole antenna with a 0.1 THz resonance frequency is designed to efficiently couple an incident terahertz beam at 0.1 THz to the plasmonic photomixer (Figure 20). A terahertz choke is connected to the plasmonic contact electrodes to route the IF photocurrent out of the plasmonic photomixer [105]. It is made up of four alternating high-impedance and low-impedance quarter-wavelength transmission lines and is designed to provide a high resistance and low

46

reactance loading to the terahertz antenna at 0.1 THz while keeping a 50 Ω impedance at GHz-range IF frequencies.

## 5.1.2 Characterization of the first generation heterodyne terahertz receiver based on a plasmonic photomixer with a dipole antenna

The first generation heterodyne terahertz receiver is fabricated on a LT-GaAs substrate. The fabrication process starts with two groups of 30 μm × 30 μm plasmonic gratings, separated by 1 μm, patterned by electron beam lithography, followed by Ti/Au (5/45 nm) deposition and liftoff. A 300 nm thick of $Si_3N_4$ anti-reflection coating layer is then deposited using plasma enhanced chemical vapor deposition. Then contact vias are patterned by optical photolithography and etched through the $Si_3N_4$ layer by dry plasma etching. Finally, the antenna, transmission line, and terahertz choke are patterned using optical photolithography, followed by Ti/Au (50/400 nm) deposition and liftoff. Figure 21 shows the microscope image of the first generation prototype heterodyne terahertz receiver with a dipole antenna and the scanning electron microscope (SEM) image of the plasmonic contact electrode gratings.
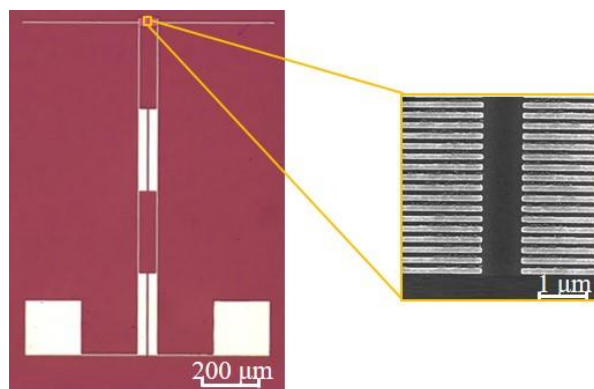


Figure 21. Microscope image of the first generation heterodyne terahertz receiver prototype based on a plasmonic photomixer with a dipole antenna and the scanning electron microscope (SEM) image of the plasmonic contact electrodes.

The first generation heterodyne terahertz receiver prototype is characterized in response to radiation from a Gunn oscillator in W-band (Millitech GDM-10) and its IF output is monitored on a spectrum analyzer. Figure 22 shows the experimental setup. The outputs of two wavelength-tunable, distributed-feedback (DFB) lasers with 783 nm and 785 nm center wavelengths (TOPTICA #LD-0783-0080-DFB-1 and #LD-07835-0080-DFB-1) are combined and amplified to provide the optical pump beam with a tunable beating frequency from 0 to 2 THz. A pellicle is placed along the optical beam path to monitor the optical pump spectrum by an optical spectrum analyzer. The polarization of the optical pump beam and the Gunn Oscillator radiation are set to be perpendicular to the plasmonic gratings and along the dipole antenna axis, respectively.
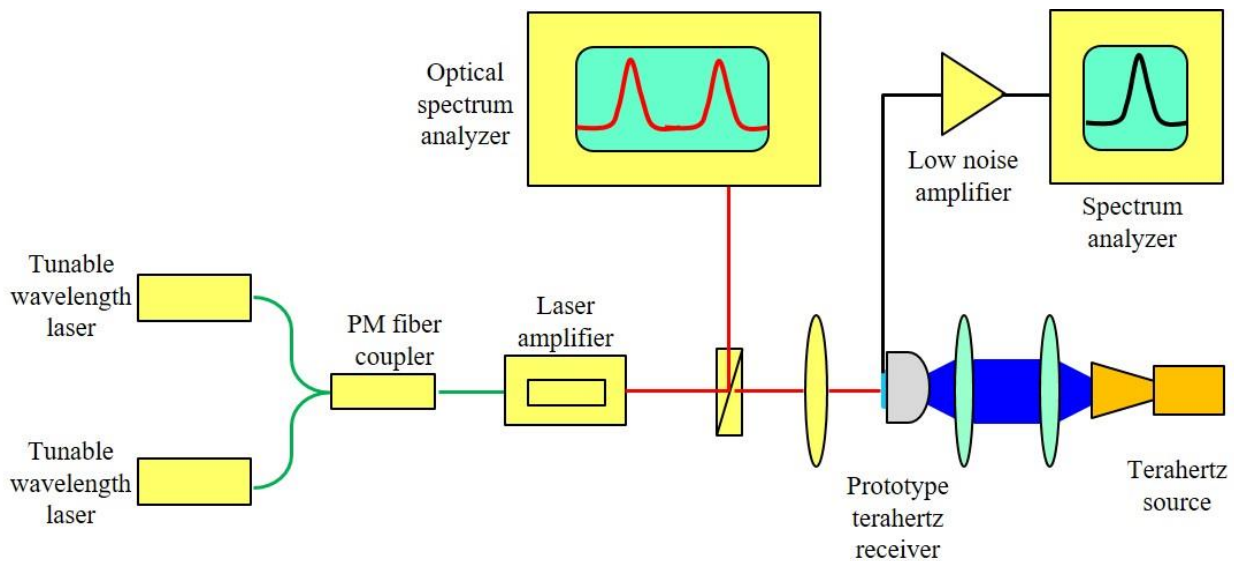


Figure 22. Experimental setup used for characterizing the heterodyne terahertz receiver prototypes.

For the first proof of concept, the radiation from the Gunn oscillator is set to be at around 97 GHz. Figure 23 shows the observed IF spectrum, while tuning the beating frequency of the optical pump lasers from 95.5 GHz to 98.5 GHz. The results illustrate the simplicity of frequency scanning through the designed plasmonic heterodyne receiver.
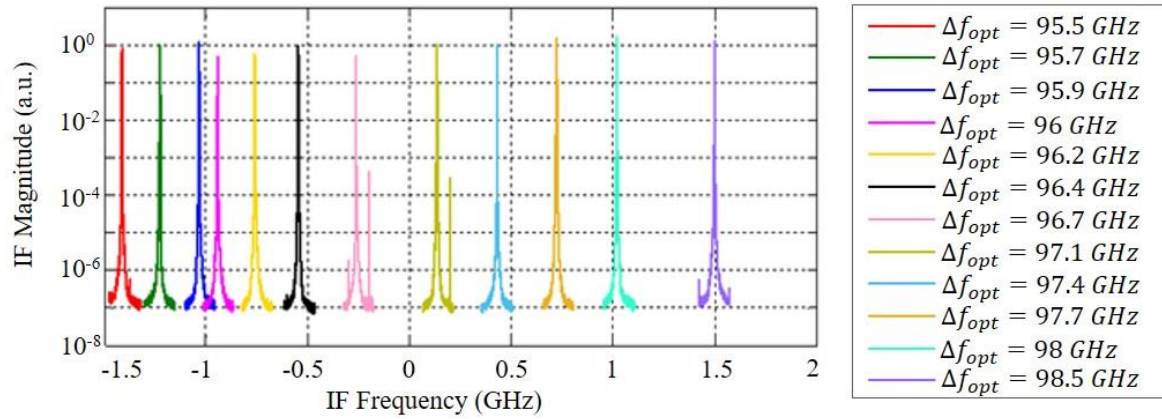
Figure 23. IF spectrum measurements while tuning the optical pump beating frequency of the first generation heterodyne terahertz receiver

Similar to the conventional heterodyne terahertz receivers, the detection sensitivity of the presented heterodyne terahertz receiver based on plasmonic photomixers is dependent on the optical local oscillator power level. Figure 24 shows the dependence of the measured IF power and noise power levels on the optical pump power level. As expected, the IF power level has a quadratic relation with the optical pump power level (Figure 24 (a)). This is because the IF current is linearly proportional to the photo-generated carrier density, which is linearly proportional to the optical pump power level. Also, since the presented photomixer is symmetrically pumped, the dominant noise mechanism is Johnson-Nyquist noise. As a result, the noise current has a square-root relation with the photoconductive material's conductivity, which is linearly proportional to the photo-generated carrier concentration. Therefore, the noise power level is linearly proportional to the optical pump power level, as shown in Figure 24 (b).

In conclusion, the detection sensitivity of the presented heterodyne terahertz received based on plasmonic photomixers can increase as the optical pump power increases. At a 500 mW optical pump power, the first generation heterodyne terahertz receiver prototype offers up to 68 dB signal-

49

to-noise ratio at room temperature (Figure 25 (a)). Moreover, the linearity of the first generation heterodyne terahertz receiver prototype is characterized by using a fully-calibrated W-band attenuator to attenuate the incident radiation on the receiver. The measurement results indicate a high linearity response with respect to the incident terahertz power level over more than 50 dB range (Figure 25 (b)).
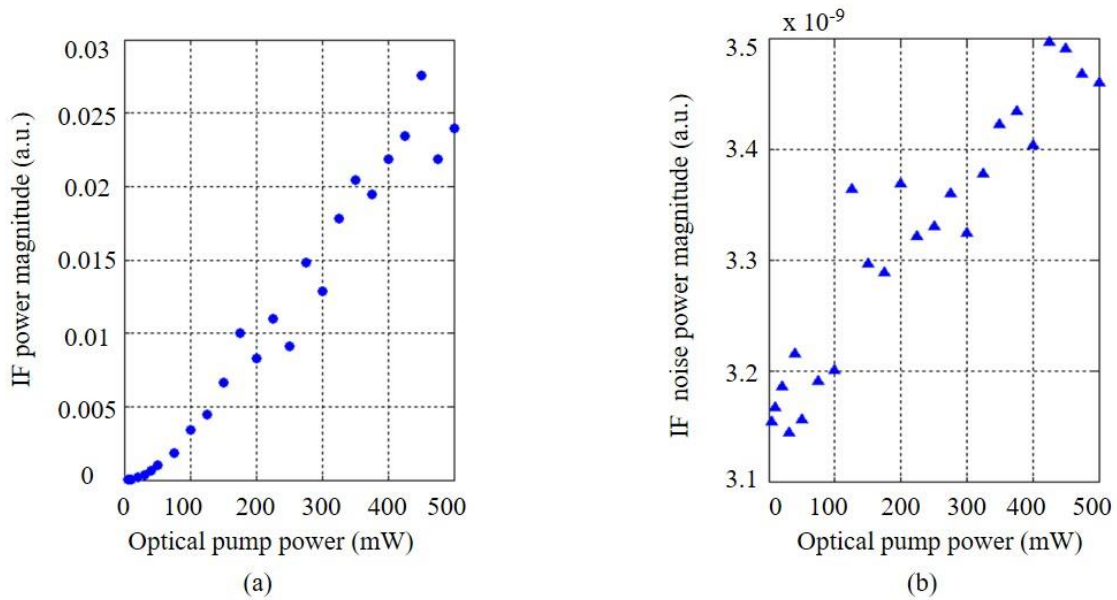


Figure 24. Characterization of the detection sensitivity of the first generation heterodyne terahertz receiver based on a plasmonic photomixer with a dipole antenna. (a) The IF power level has a quadratic dependence on the optical pump power level; (b) the noise power level has a linear dependence on the optical pump power level.
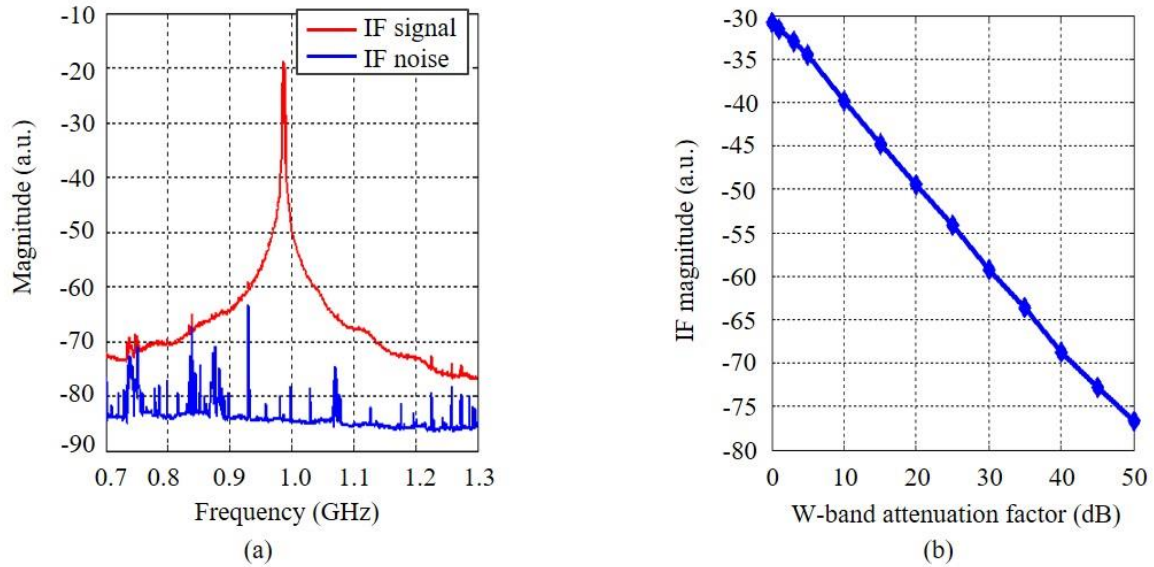
Figure 25. (a) Signal-to-noise ratio of the first generation heterodyne receiver prototype at a 500 mW optical pump power. (b) Dynamic range of the heterodyne receiver at a 300 mW optical pump power.

Another important characteristic of the presented heterodyne receiver concept is that it can offer high spectral resolution. This is because the spectral resolution of the presented heterodyne receiver is directly determined by the linewidth and stability of the optical pump beams. In order to characterize the spectral resolution of the first generation heterodyne terahertz receiver, a Ti: sapphire mode-locked laser is used as the optical local oscillator, as shown in Figure 26. The Ti: sapphire mode-locked laser used for this measurement has a stable repetition rate of 75 MHz in the time-domain, providing a stable frequency comb in the frequency-domain with a 75 MHz separation between two adjacent comb lines. Any comb line pair that has a frequency separation of ~97 GHz can serve as a pump for the heterodyne receiver and generate an IF signal at ~1 GHz. By monitoring the IF signal on a spectrum analyzer, an IF linewidth of ~2 kHz is measured under the 75 MHz frequency comb pump beam (Figure 27), implying a spectral resolution of 2 KHz for the first generation heterodyne terahertz receiver prototype.
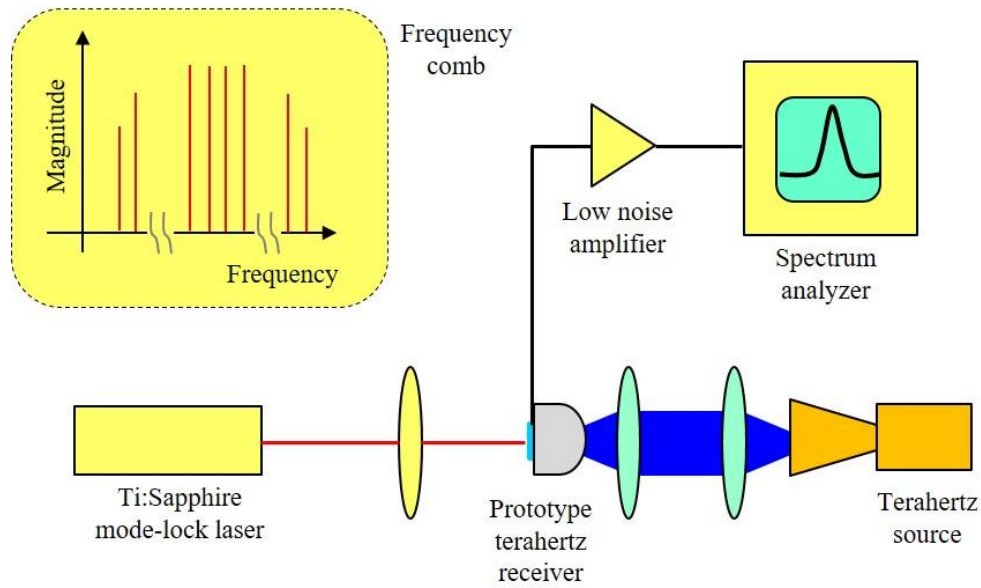
Figure 26. Experimental setup for characterizing the spectral resolution of the first generation heterodyne terahertz receiver.
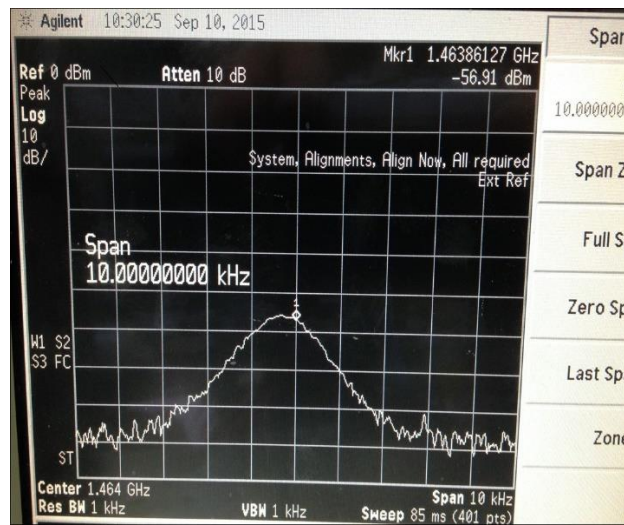


Figure 27. Measured IF spectrum while using a narrow-linewidth Ti:sapphire mode-locked laser to pump the heterodyne terahertz receiver.

## 5.2 Second Generation Heterodyne Terahertz Receiver based on a Plasmonic Photomixer with a Logarithmic Spiral Antenna

Inspired by the successful demonstration of the first generation heterodyne terahertz receiver based on a plasmonic photomixer integrated with a dipole antenna, a second generation heterodyne terahertz receiver based on a plasmonic photomixer integrated with a logarithmic spiral antenna is designed for broadband operation.

### 5.2.1 Design of the second generation heterodyne terahertz receiver based on a plasmonic photomixer with a logarithmic spiral antenna



Figure 28. Schematic diagram of the second generation heterodyne terahertz receiver based on a plasmonic photomixer integrated with a logarithmic spiral antenna.

The second generation heterodyne terahertz receiver is composed of a heterodyne photomixer with plasmonic contact electrode gratings integrated with a logarithmic spiral antenna, as shown in Figure 28. The spiral antenna is designed to have an inner radius of 5 μm and an outer radius of 303 μm. The plasmonic gratings cover an active area of 8 μm × 8 μm and consist of gold electrodes with 50 nm thickness, 200 nm pitch, and 100 nm spacing. A 300 nm thick silicon nitride layer is

53

used as an anti-reflection coating. This design of plasmonic gratings can provide a high optical power transmission (~ 85%) and a strong plasmonic enhancement when excited by a TM polarized optical pump beam at 784 nm wavelength.

### 5.2.2 Characterization of the second generation heterodyne terahertz receiver based on a plasmonic photomixer with a logarithmic spiral antenna

A prototype of the second generation heterodyne terahertz receiver based on a plasmonic photomixer with a logarithmic spiral antenna is fabricated on a LT-GaAs substrate (Figure 29) and characterized in the same optical setup shown in Figure 22.
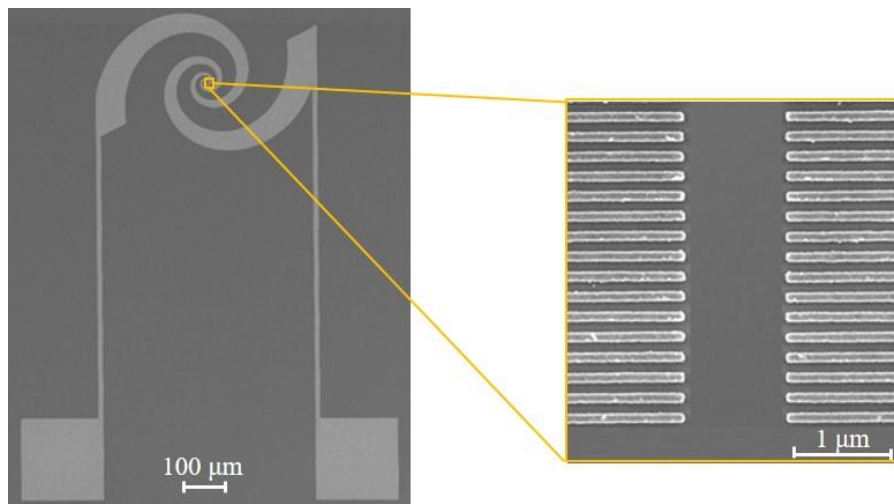


Figure 29. Scanning electron microscope (SEM) images of the second generation heterodyne terahertz receiver based on a plasmonic photomixer with a logarithmic spiral antenna.

This second generation heterodyne terahertz receiver is characterized in response to continuous-wave radiations at 0.1 THz and 0.55 THz, respectively. A gunn oscillator is used to provide the continuous-wave radiation at around 0.1 THz, and a chain of frequency multipliers are connected to the output of the Gunn oscillator to provide continuous-wave radiation up to 0.55 THz. The results indicate broadband terahertz detection in the 0.1 – 0.55 THz frequency range (Figure 30).

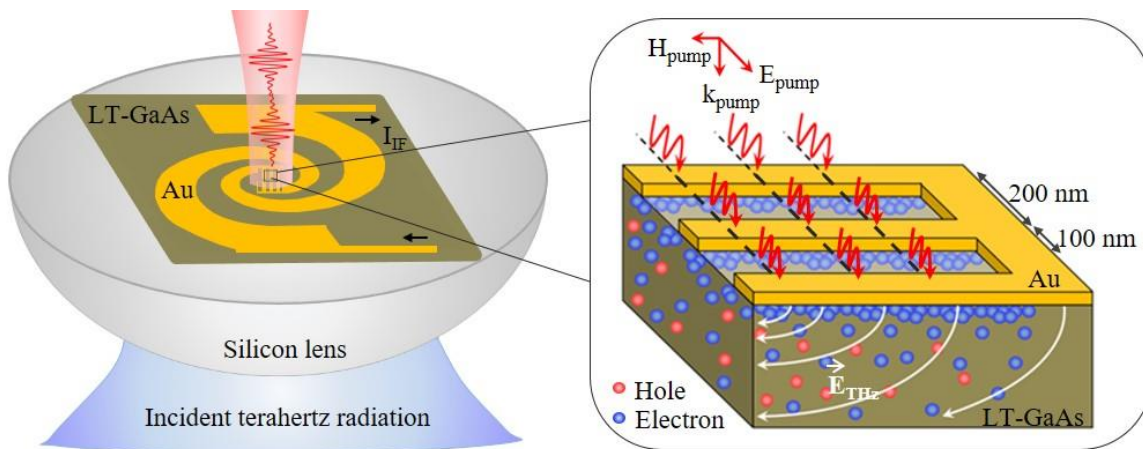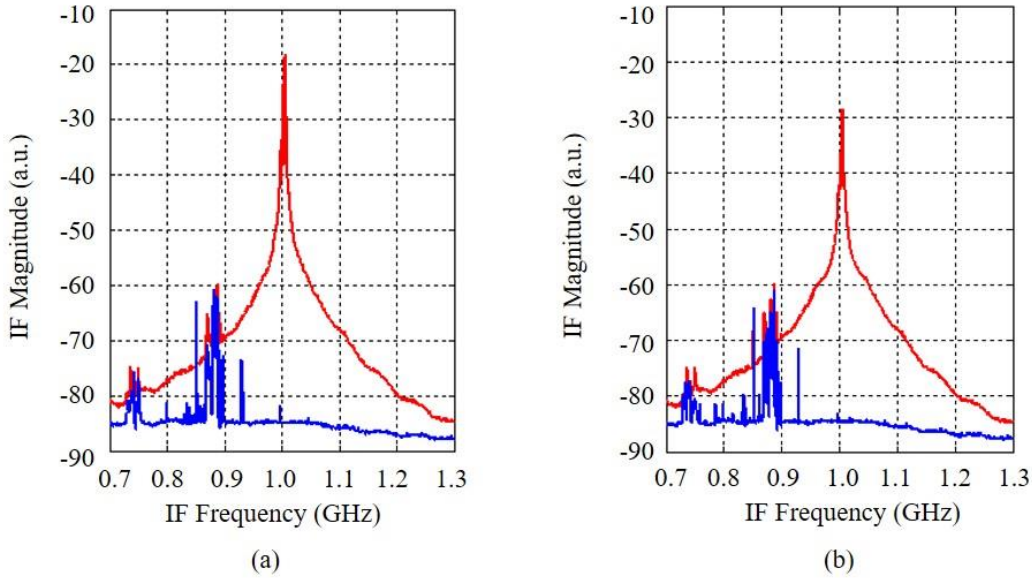Figure 30. Characterization of the second generation heterodyne terahertz receiver prototype based on a plasmonic photomixer with a logarithmic spiral antenna. The red curves show the measured IF power at 1 GHz, and the blue curves show the background noise in the absence of the incident terahertz radiation, under optical local oscillator illumination. The measured spectra at 0.1 THz and 0.55 THz are shown in (a) and (b), respectively.

The broad operation bandwidth of the second generation heterodyne terahertz receiver prototype is characterized by use of a WR9.0 modular amplifier / multiplier chain (AMC) made by Virginia Diode Inc. (VDI), which up-converts the frequency of a synthesizer to provide CW terahertz radiation from 82 GHz to 750 GHz. Figure 31 (a) shows the measured IF power at different frequency ranges and Figure 31 (b) shows the radiation power of the VDI WR9.0 AMC module provided by the manufacturer. The measurement results indicate a relatively linear relation between the measured IF power and incident terahertz power over a broad terahertz frequency range. Fluctuations in the measured IF power are due to the fluctuations in the synthesizer output power fed to the VDI WR9.0 AMC module. This is also evident from the fact that the measured IF spectra remain unchanged over all of the measured frequency bands.
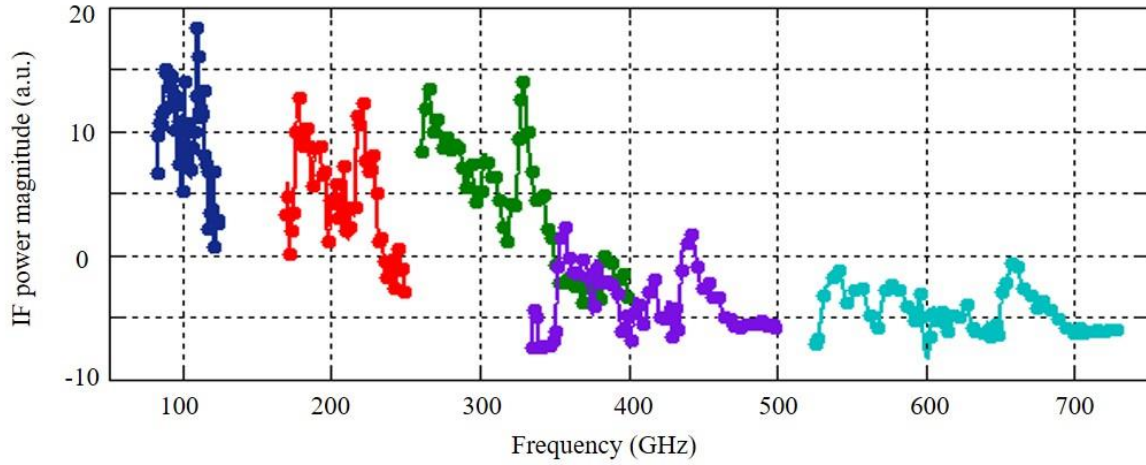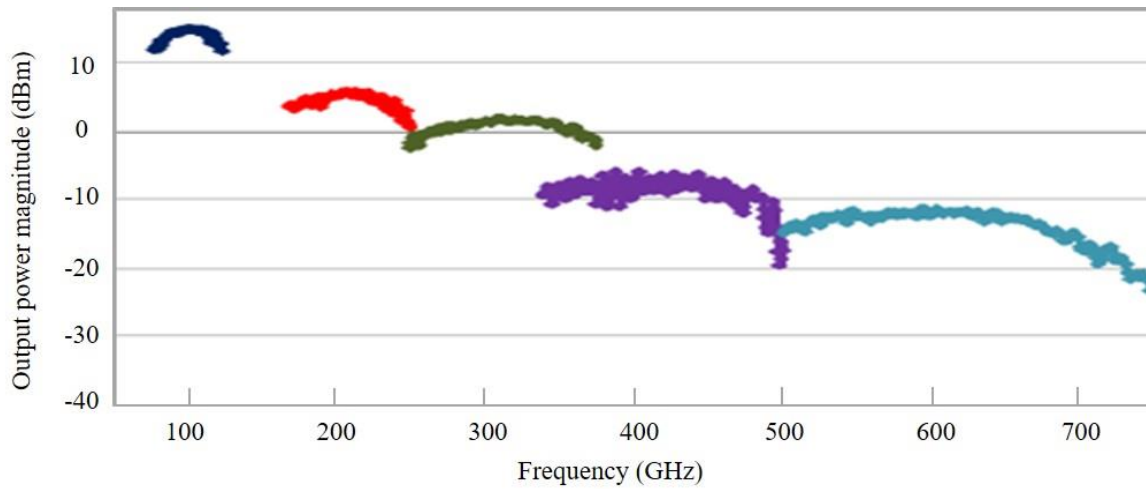
Figure 31. Characterization of the bandwidth of the second generation plasmonic heterodyne terahertz receiver prototype over 80-750 GHz by use of a VDI WR9.0 modular amplifier / multiplier chain. The measured IF power plotted in logarithmic scale and the output power from the VDI AMC module, provided by the manufacturer [118], are shown in (a) and (b), respectively.

## 5.3  Conclusion

A novel architecture for heterodyne terahertz receivers based on plasmonic photomixers is presented, which replaces the terahertz local oscillator and mixer of conventional heterodyne

terahertz receivers with an optical local oscillator and plasmonic photomixer, respectively. As a result, the bandwidth and sensitivity of the presented heterodyne terahertz receiver is not limited by the narrow frequency tunability and low output power of existing terahertz sources. Two generations of receivers are designed and characterized to experimentally demonstrate the large dynamic range and broadband operation bandwidth offered by the presented heterodyne terahertz receiver architecture.

# CHAPTER 6

# Conclusions and Future Work

Two types of high sensitivity terahertz receivers based on plasmonic photoconductors are studied and significant performance enhancement compared to the state-of-the-art is demonstrated. It is experimentally demonstrated that incorporating plasmonic contact electrodes in photoconductive terahertz receivers reduces the transport path length of the majority of the photocarriers to the contact electrodes, enabling high quantum efficiency and ultrafast operation simultaneously. Additionally, a new scheme for implementing heterodyne terahertz receivers is presented, which replaces the terahertz local oscillator and mixer used in conventional heterodyne terahertz receivers with two wavelength-tunable optical sources and a plasmonic photomixer, respectively. As a result, the performance of the presented heterodyne terahertz receivers is not affected by the low radiation power and limited frequency range of existing terahertz sources and the limited operation bandwidth of existing terahertz mixers. Two prototype heterodyne terahertz receivers based on plasmonic photomixers are designed for operation at different terahertz frequency ranges, fabricated and characterized, indicating significantly broader operation bandwidths and dynamic ranges offered by the presented plasmonic heterodyne terahertz receiver concept.

To further improve the performance of the terahertz receivers based on plasmonic photoconductors, the terahertz coupling efficiency is a very important factor that needs to be enhanced. In this regard,

using large area device architectures or terahertz antenna arrays are potential ways that can significantly enhance terahertz wave coupling to the plasmonic terahertz receivers. Another possible direction worth exploring is use of terahertz waveguides. A carefully-designed tapered waveguide connected to a horn antenna can significantly enhance terahertz wave coupling to the plasmonic terahertz receivers.

# BIBLIOGRAPHY

# BIBLIOGRAPHY

[1] D. Graham-Rowe, "Terahertz takes to the stage," *Nat.Photonics* **1**, 75 − 77 (2007).

[2] M. C. Kemp, et al. "Security applications of terahertz technology," *Proc. of SPIE* **5070**, 44 − 52 (2003).

[3] D. Arnone, C. Ciesla and M. Pepper, "Terahertz imaging comes into view," *Physics World*, 35 − 40 (2003).

[4] J. A. Zeitler, et al. "Terahertz pulsed spectroscopy and imaging in the pharmaceutical setting − a review," *Journal of Pharmacy and Pharmacology* **59**, 209 − 223 (2007).

[5] A. Y. Pawar, et al. "Terahertz technology and its applications," *Drug Invention Today* **5**, 157 − 163 (2013).

[6] D. H. Auston, et al. "Picosecond optoelectronic detection, sampling, and correlation measurements in amorphous semiconductors," *Appl. Phys. Lett* **37**, 371 − 373 (1980).

[7] D. H. Auston, "Subpicosecond electro-optic shock waves," *Appl. Phys. Lett* **43**, 713 − 715 (1983).

[8] P. R. Smith, D. H. Auston, and M. C. Nuss, "Subpicosecond photoconducting dipole antennas," *IEEE J. of Quantum Electron.* **24**, 255 − 260 (1988).

[9] X. Yin, et al. "Terahertz sources and detectors," *Terahertz Imaging for Biomedical Application: Pattern Recognition and Tomographic Reconstruction*, (2012).

[10] N. S. Ginzburg, et al. "Powerful terahertz free electron lasers with hybrid Bragg reflectors," *Phys. Rev. ST Accel. Beams* **14**, 042001 − 1 − 9 (2011).

[11] G. P. Williams, "High-power terahertz synchrotron sources," *Phil. Trans. R. Soc. Lond. A* **362**, 403 − 414 (2004).

[12] S. Y. Tochitsky, et al. "Generation of megawatt-power terahertz pulses by noncollinear difference-frequency mixing in GaAs," *J. Appl. Phys.* **98**, 026101 − 1 − 3 (2005).

[13] S. Y. Tochitsky, et al. "High-power tunable, 0.5-3 THz radiation source based on nonlinear difference frequency mixing of $CO_2$ laser lines*,*" *J. Opt. Soc. Am. B* **24**, 2509 − 2516 (2007).

[14] S. Preu, et al. "Tunable, continuous-wave terahertz photomixer sources and applications," *J. Appl. Phys.* **109**, 061301 − 1 − 55 (2011).

[15] K. Liu, et al. "Terahertz radiation from InAs induced by carrier diffusion and drift," *Phys. Rev. B.* **73**, 155330 – 1 – 6 (1992).

[16] X. Xie, J. Xu and X. C. Zhang, "Terahertz wave generation and detection from a CdTe crystal characterized by different excitation wavelengths," *Opt. Lett.* **31**, 978 - 980 (2006).

[17] J. Hebling, et al. "Generation of high-power terahertz pulses by tilted-pulse-front excitation and their application possbilities," *J. Opt. Soc. Am. B* **25**, B6 – B 19 (2008).

[18] Y. S. Lee, et al. "Generation of narrow-band terahertz radiation via optical rectification of femtosecond pulses in periodically poled lithium niobate," *Appl. Phys. Lett.* **76**, 2505 – 2507 (2000).

[19] K. A. McIntosh, et al. "Terahertz photomixing with diode lasers in low-temperature-grown GaAs," *Appl. Phys. Lett.* **67**, 3844 – 3846 (1995).

[20] C. W. Berry, et al. "Significant performance enhancement in photoconductive terahertz optoelectronics by incorporating plasmonic contact electrodes," *Nat. Commun.* **4**, 1622 (2013).

[21] C. W. Berry, et al. "High power terahertz generation using 1550 nm plasmonic photomixers," *Appl. Phys. Lett.* **105**, 011121 (2014).

[22] S. -H. Yang, et al. "7.5% optical-to-terahertz conversion efficiency offered by photoconductive emitters with three-dimensional plasmonic contact electrodes," *IEEE Trans. THz Sci. Technol.* **4**, 575 – 581 (2014).

[23] N. T. Yardimci, et al. "High power terahertz generation using large area plasmonic photoconductive emitters," *IEEE Trans. THz Sci. Technol.* **5**, 223 – 229 (2015).

[24] M. G. Krishna, S. D. Kshirsagar and S. P. Tewari, "Terahertz Emitters, Detectors and Sensors: Current Status and Future Prospects, Photodetectors, Dr. Sanka Gateva (Ed.)," ISBN: 978 – 953 – 51 – 0358 – 5 (2012).

[25] M. van Exter, C. Fattinger, and D. Grischkowsky, "Terahertz time-domain spectroscopy of water vapor," *Opt. Lett.* **14**, 1128 – 1130 (1989).

[26] N. Karpowicz, et al. "Comparison between pulsed terahertz time-domain imaging and continuous wave terahertz imaging," *Semicond. Sci. Technol.* **20**, S293 – S299 (2005).

[27] W. L. Chan, J. Deibel and D. M. Mittleman, "Imaging with terahertz radiation," *Rep. Prog. Phys.* **70**, 1325 – 1379 (2007).

[28] F. Sizov, and A. Rogalski, "THz detectors," *Prog. Quant. Electron.* **34**, 278 – 347 (2010).

[29] P. L. Richards, "Bolometers for infrared and millimeter waves," *J. Appl. Phys.* **76**, 1 – 24 (1994).

[30] A. Hossain, and M. H. Rashid, "Pyroelectric detectors and their applications," *IEEE Trans. Ind. Appl.* **27**, 824 – 829 (1991).

[31] M. J. E. Golay, "The theoretical and practical sensitivity of the Pneumatic infrared detector," *Rev. Sci. Instrum.* **20**, 816 – 820 (1949).

[32] K. Yamashita, A. Murata, and M. Okuyama, "Miniaturized infrared sensor using silicon diaphragm based on Golay cell," *Sensor. Actuat A* **66**, 29 – 32 (1998).

[33] A. D. Turner, et al. "Silicon nitride micromesh bolometer array for submillimeter astrophysics," *Appl. Opt.* **40**, 4921 – 4932 (2001).

[34] H. –W. Hubers, "Terahertz heterodyne receivers," *IEEE J. Sel. Topics Quantum Electron.* **14**, 378 – 391 (2008).

[35] T. W. Crowe, et al. "GaAs Schottky Diodes for THz mixing applications," *Proc. IEEE* **80**, 1827 – 1841 (1992).

[36] A. Maestrini, et al. "Schottky diode-based terahertz frequency multipliers and mixers," *C. R. Physics* **11**, 480 – 495 (2010).

[37] A. Van der Ziel, "Infrared detection and mixing in heavily doped Schottky-barrier diodes," *J. Appl. Phys.* **47**, 2059 – 2068 (1976).

[38] T. W. Crowe, et al. "Opening the terahertz window with integrated diode circuits," *IEEE J. Solid-state Circuits* **40**, 2104 – 2110 (2005).

[39] A. H. Dayem, and R. J. Martin, "Quantum interaction of microwave radiation with tunneling between superconductors," *Phys. Rev. Lett.* **8**, 246 – 248 (1962).

[40] P. L. Richards, et al. "Quasiparticle heterodyne mixing in SIS tunnel junctions," *Appl. Phys. Lett.* **34**, 345 – 347 (1979).

[41] J. R. Tucker, and M. J. Feldman, "Quantum detection at millimeter wavelengths," *Rev. Mod. Phys.* **57**, 1055 -1113 (1985).

[42] K. H. Gundlach, and M. Schicke, "SIS and bolometer mixers for terahertz frequencies," *Supercond. Sci. Technol.* **13**, R171 – R187 (2000).

[43] G. J. Dolan, T. G. Phillips, and D. P. Woody, "Low-noise 115-GHz mixing in superconducting oxide-barrier tunnel junctions," *Appl. Phys. Lett.* **34**, 347 – 349 (1979).

[44] P. K. Tien, and J. P. Gordon, "Multiphoton process observed in the interaction of microwave fields with the tunneling between superconductor films," *Phys. Rev.* **129**, 647 – 651 (1963).

[45] W. J. Skocpol, M. R. Beasly, and M. Tinkham, "Self-heating hotspots in superconducting thin-film microbridge," *J. Appl. Phys.* **45**, 4054 -4066 (1974).

[46] E. M. Gershenzon, et al. "Millimeter and submillimeter range mixer based on electronic heating of superconducting films in the resistive state," *Superconductivity* **3**, 1582 – 1597 (1990).

[47] B. S. Karasik, et al. "Hot electron quasioptical NbN superconducting mixer," *IEEE Trans. Appl. Supercond.* **5**, 2232 – 2235 (1995).

[48] D. E. Prober, "Superconducting terahertz mixer using a transition edge micro bolometer," *Appl. Phys. Lett.* **62**, 2119 − 2121 (1993).

[49] A. Skalare, et al. "Large bandwidth and low noise in a diffusion-cooled hot-electron bolometer mixer," *Appl. Phys. Lett.* **68**, 1558 − 1560 (1996).

[50] G. Chattopadhyay, "Sensor technology at submillimeter wavelengths for space applications," *International Journal on Smart Sensing and Intelligent Systems*, **1**, 1 (2008).

[51] N. G. Douglas, *Millimeter and submillimeter wavelength lasers*. Berlin, Germany: Springer-Verlag (1989).

[52] M. Tani, et al. "Efficient electro-optic sampling detection of terahertz radiation via Cherenkov phase matching," *Opt. Express.* **19**, 19901 − 19906 (2011).

[53] A. Tomasino, et al. "Wideband THz time domain spectroscopy based on optical rectification and electro-optic sampling," *Sci. Rep.* **3**, 3116 (2013).

[54] D. H. Auston, and A. M. Glass, "Optical generation of intense picosecond electrical pulses," *Appl. Phys. Lett.* **20**, 398 − 399 (1972).

[55] J. A. Valdmanis, G. Mourou, and C. W. Gabel, "Picosecond electro-optic sampling system," *Appl. Phys. Lett.* **41**, 211 − 212 (1982).

[56] P. Uhd Jepsen, et al. "Detection of THz pulses by phase retardation in lithium tantalate," Phys. Rev. E. 53, R3052 − R3054 (1996).

[57] Q. Wu, T. D. Hewitt, and X.-C. Zhang, "Two-dimensional electro-optic imaging of THz beams," *Appl. Phys. Lett.* **69**, 1026 − 1028 (1996).

[58] A. Nahata, A. S. Weling, and T. F. Heinz, "A wideband coherent terahertz spectroscopy system using optical rectification and electro-optic sampling," *Appl. Phys. Lett.* **69**, 2321 − 2323 (1996).

[59] C. Winnewisser, et al. "Electro-optic detection of THz radiation in LiTaO3, LiNbO3 and ZnTe," *Appl. Phys. Lett.* **70**, 3069 − 3071 (1997).

[60] G. Gallot, et al. "Measurements of the THz absorption and dispersion of ZnTe and their relevance to the electro-optic detection of THz radiation," Appl. Phys. Lett. 74, 3450 − 3452 (1999).

[61] Y. C. Shen, et al. "Generation and detection of ultrabroadband terahertz radiation using photoconductive emitters and receivers," Appl. Phys. Lett. 85, 164 − 166 (2004).

[62] M. Venkatesh, et al. "Optical characterization of GaAs photoconductive antennas for generation and detection of terahertz radiation," *Opt. Mater.* **36**, 596 − 601 (2014).

[63] S. Kono, M. Tani, and K. Sakai, "Ultrabroadband photoconductive detection: comparison with free-space electro-optic sampling," Appl. Phys. Lett. 79, 898 − 900 (2001).

[64] F. Peter, et al. "Coherent terahertz detection with a large-area photoconductive antenna," *Appl. Phys. Lett.* **91**, 40 − 42, (2007).

[65] Y. Cai, et al, "Coherent terahertz radiation detection: Direct comparison between free-space electro-optic sampling and antenna detection," *Appl. Phys. Lett.* **73**, 444 – 446 (1998).

[66] J. S. Blakemore, "Semiconducting and other major properties of gallium arsenide," *J. Appl. Phys.* **53**, R123 – R181 (1982).

[67] J. Pozhela, and A. Reklaitis, "Electron transport properties in GaAs at high electric fields," *Solid State Electron* **23**, 927 – 933 (1980).

[68] Z. Piao, M. Tani, and K. Sakai, "Carrier dynamics and terahertz radiation in photoconductive antennas," *Jpn. J. Appl. Phys.* **39**, 96 – 100 (2000).

[69] K. Ezdi, et al. "A hybrid time-domain model for pulsed terahertz dipole antennas," *J. European Opt. Soc.* **4**, 09001 (2009).

[70] E. R. Brown, F. W. Smith, and K. A. McIntosh, "Coherent millimeter-wave generation by heterodyne conversion in low-temperature-grown GaAs photoconductors," *J. Appl. Phys.* **73**, 1480 – 1484 (1993).

[71] E. R. Brown, "Terahertz generation by photomixing in ultrafast photoconductors," *Int. J. High Speed Electronics and Systems*, **13**, 497 – 545 (2003).

[72] C. W. Berry, and M. Jarrahi, "Principles of impedance matching in photoconductive antennas," *J. Infrared, Millimeter & Terahertz Waves* **33**, 1182-1189 (2012).

[73] L. Hou, W. Shi, and S. Chen, "Noise analysis and optimization of terahertz photoconductive emitters," *IEEE J. Selected Topics in Quantum Electronics* **19**, 8401305 (2013).

[74] J. S. Weiner, and P. Y. Yu, "Free carrier lifetime in semi-insulating GaAs from time-resolved band-to-band photoluminescence," *J. Appl. Phys.* **55**, 3889-3891(1984).

[75] R. K. Ahrenkiel, et al, "Recombination lifetime of $In_{0.53}Ga_{0.47}As$ as a function of doping density," *Appl. Phys. Lett.* **72**, 3470 – 3472 (1998).

[76] N. Chimot, et al, "Terahertz radiation from heavy-ion-irradiated $In_{0.53}Ga_{0.47}As$ photoconductive antenna excited at 1.55um," *Appl. Phys. Lett.* **87**, 193510 (2005).

[77] T. P. Pearsall, et al. "The carrier mobilities in $Ga_{0.47}In_{0.53}As$ grown by organo-metallic CVD and liquid-phase epitaxy," *Journal of Crystal Growth* **54**, 127 – 131 (1981).

[78] K. A. McIntosh, et al. "Investigation of ultrashort photocarrier relaxation times in low-temperature-grown GaAs," Appl. Phys. Lett. 70, 118412 (1997).

[79] J. Johnson, "Thermal agitation of electricity in conductors," *Phys. Rev.* **32**, 97 (1928).

[80] H. Nyquist, "Thermal agitation of electric charge in conductors," *Phys. Rev.* **32**, 110 (1928).

[81] N. Wang, M. Jarrahi, "Noise Analysis of Photoconductive Terahertz Detectors," *J. Infrared, Millim. Terahertz Waves*, **34**, 519-528 (2013).

[82] J. A. Porto, F. J. Garcia-Vidal, and J. B. Pendry, "Transmission Resonances on Metallic Gratings with Very Narrow Slits," *Phys. Rev. Lett.* **83**, 2845 – 2848 (1999).

[83] Z. Sun, Y. S. Jung, and H. K. Kim, "Role of surface plasmons in the optical interaction in metallic gratings with narrow slits," *Appl. Phys. Lett.* **83**, 3021 – 3023 (2003).

[84] W. L. Barnes, A. Dereux, and T. W. Ebbesen, "Surface plasmon subwavelength optics," *Nature* **424**, 824 – 830 (2003).

[85] C. Genet and T. W. Ebbesen, "Light in tiny holes," *Nature* **445**, 39 – 46 (2007).

[86] B –Y. Hsieh, M. Jarrahi, "Analysis of periodic metallic nano-slits for efficient interaction of terahertz and optical waves at nano-scale dimensions," *J. Appl. Phys.* **109**, 084326 (2011).

[87] C. W. Berry, and M. Jarrahi, "Plasmonic-enhanced localization of light into photoconductive antennas," *Proc. Conference of Laser and Electro-Optics (CLEO)*, Paper CFI2 (2010).

[88] J. F. O'Hara, et al, "Enhanced terahertz detection via ErAs:GaAs nanoisland superlattices," *Appl. Phys. Lett.* **88**, 251119 (2006).

[89] F. G. Sun, G. A. Wagoner, and X.-C. Zhang, "Measurement of free-space terahertz pulses via long-lifetime Photoconductors," *Appl. Phys. Lett.* **67**, 1656-1658 (1995).

[90] H. Roehle, et al. "Next generation 1.5 um terahertz antennas: mesa-structuring of InGaAs/InAlAs photoconductive layers," *Opt. Express* **18**, 2296 – 2301 (2010).

[91] Z. D. Taylor, et al. "Resonant-optical-cavity photoconductive switch with 0.5% conversion efficiency and peak power," *Opt Lett.* **31**, 1729 – 1731 (2006).

[92] J. H. Kim, A. Polley, and S. E. Ralph, "High efficiency terahertz photoconducting sources by use of spatially shaped excitation," *Opt. Lett.* **30**, 2490 – 2492 (2005).

[93] M. Tani, K.-S. Lee, and X.-C. Zhang, "Detection of terahertz radiation with low-temperature-grown GaAs-based photoconductive antenna using 1.55um probe," *Appl. Phys. Lett.* **77**, 1396 – 1398 (2000).

[94] T.-A. Liu, et al. "Ultrabroadband terahertz field detection by photoconductive antennas based on multi-energy arsenic-ion-implanted GaAs and semi-insulating GaAs," *Appl. Phys. Lett.* **83**, 1322 – 1324 (2003).

[95] M. Suzuki, and M. Tonouchi, "Fe-implanted InGaAs photoconductive terahertz detectors triggered by 1.56um femtosecond optical pulses," *Appl. Phys. Lett.* **86**, 163504 (2005).

[96] T. Kataoka, et al. "Improved sensitivity of terahertz detection by GaAs photoconductive antennas excited at 1560 nm," *Appl. Phys. Lett.* **97**, 201110 (2010).

[97] E. Castro-Camus, et al. "Polarization-sensitive terahertz detection by multicontact photoconductive receivers," *Appl. Phys. Lett.* **86**, 254102 (2005).

[98] S. Liu, X. Shou, and A. Nahata, "Coherent detection of multiband terahertz radiation using a surface plasmon-polariton based photoconductive antenna," *IEEE Trans. Terahertz Sci. Technol.* **1**, 412 − 415 (2011).

[99] B. Heshmat, et al. "Nanoplasmonic terahertz photoconductive switch on GaAs," *Nano Lett.* **12**, 6255 − 6259 (2012).

[100] P. V. Gerwen, et al. "Nanoscaled interdigitated electrode arrays for biochemical sensors," *Sensor Actuat. B* **49**, 73 − 80 (1998).

[101] C. W. Berry, N. Wang, M. R. Hashemi, M. Unlu, M. Jarrahi, "Significant Performance Enhancement in Photoconductive Terahertz Optoelectronics by Incorporating Plasmonic Contact Electrodes," *Nat. Commun.* **4**, 1622 (2013).

[102] P. H. Siegel. "Terahertz technology in biology and medicine," *2004 IEEE MITT-S Intl. Microwave Symp.*, 1575 − 1578 (2004).

[103] S. Gulkis, et al. "Remote sensing of a comet at millimeter and submillimeter wavelengths from an orbiting spacecraft," *Planetary Space Sci.* **55**, 1050 − 1057 (2007).

[104] S. Verghese, et al. "A photomixer local oscillator for a 630-GHz heterodyne receiver," *IEEE Microw. Guided Wave Lett* **9**, 245 − 247 (1999).

[105] S. M. Duffy, et al. "Accurate modeling of dual dipole and slot elements used with photomixers for coherent terahertz output power," *IEEE Trans. Microw. Theory Techn.* **49**, 1032 − 1038 (2001).

[106] I. S. Gregory, et al. "Analysis of photomixer receivers for continuous-wave terahertz radiation," *Appl. Phys. Lett.* **91**, 154103 (2007).

[107] I. S. Gregory, et al. "Resonant dipole antennas for continuous-wave terahertz photomixers," *Appl. Phys. Lett.* **85**, 1622 − 1624 (2004).

[108] J. E. Bjarnason, et al. "ErAs:GaAs photomixer with two-decade tenability and 12uW peak output power," *Appl. Phys. Lett.* **85**, 3983 − 3985 (2004).

[109] E. Peytavit, et al. "Milliwatt-level output power in the sub-terahertz range generated by photomixing in a GaAs photoconductor," *Appl. Phys. Lett.* **99**, 223508 (2011).

[110] S. Gregory, et al. "Optimization of photomixers and antennas for continuous-wave terahertz emission," *IEEE J. Quantum Electron.* **41**, 717 − 728 (2005).

[111] J. S. Blakemore, "Semiconducting and other major properties of gallium arsenide," *J. Appl. Phys.* **53**, 123 −181 (1982).

[112] J. Pozhela, and A. Reklaitis, "Electron transport properties in GaAs at high electric fields," *Solid State Electron.* **23**, 927 − 933 (1980).

[113] T. Minamikawa, et al. "Real-time determination of absolute frequency in continuous-wave terahertz radiation with a photocarrier terahertz frequency comb induced by an unstablized femtosecond laser," *J. Infrared, Millimeter & Terahertz Waves* **37**, 473 − 485 (2016).

[114] T. Yasui, et al. "Terahertz frequency metrology based on frequency comb," *IEEE J. Sel. Top. Quantum Electron* **17**, 191 – 201 (2011).

[115] Th. Udem, R. Holzwarth, and T. W. Hänsch, "Optical frequency metrology," *Nature* **416**, 233 – 237 (2002).

[116] N. Wang, M. Jarrahi, "Heterodyne terahertz detection with plasmonic photomixers," *IEEE Microwave Symposium Digest*, San Francisco, CA, May 22 – 27 (2016).

[117] N. Wang, M. Jarrahi, "Broadband heterodyne terahertz detector based on plasmonic photomixing," *Proc. International Conference on Infrared, Millimeter, and Terahertz Waves,* Denmark, Denmark, September 25 – 30 (2016).

[118] "VDI WR9.0 modular amplifier / multiplier chain," Retrieved from http://vadiodes.com/~vdi/images/systems/VDI_WR9.0M-AMC_Product_Overview.pdf.